NASA

TECHNICAL NOTE

D-1611

PERFORMANCE AND SOME DESIGN ASPECTS OF

THE FOUR-STAGE SOLID-PROPELLANT ROCKET VEHICLE

USED IN THE RAM A1 FLIGHT TEST

By Jack Levine

Langley Research Center
Langley Station, Hampton, Va.

NATIONAL AERONAUTICS AND SPACE ADMINISTRATION

WASHINGTON   March 1963

NATIONAL AERONAUTICS AND SPACE ADMINISTRATION

TECHNICAL NOTE D-1611

PERFORMANCE AND SOME DESIGN ASPECTS OF

THE FOUR-STAGE SOLID-PROPELLANT ROCKET VEHICLE

USED IN THE RAM A1 FLIGHT TEST

By Jack Levine

SUMMARY

A general description, some details of mechanical design and construction, and performance (including angle of attack of the rolling last stage) of a four-stage solid-propellant rocket system used in the RAM (Radio Attenuation Measurement) A1 flight test are presented. The fourth stage attained a maximum velocity of 17,800 feet per second at an altitude of 175,000 feet. Temperature data on the nose cone are also discussed.

INTRODUCTION

As part of a general program at the Langley Research Center to investigate the effect of ionization on radio-signal attenuation during reentry flight, a free-flight test program utilizing multistage rocket-propelled vehicles was initiated. Previous investigations have been limited to ground tests and theoretical studies associated with the problem of radio transmission through the ion sheath around reentry vehicles (refs. 1 and 2) and flight tests at lower speeds with limited instrumentation (ref. 3).

The first vehicle of the RAM (Radio Attenuation Measurement) flight program, a four-stage solid-propellant rocket system, was designed to test a payload at a velocity of 18,000 feet per second and at an altitude of approximately 170,000 feet. This report presents a general description of the flight-vehicle system, some details of mechanical design and construction, vehicle performance, time-history variations of payload skin temperatures, and approximate angles of attack of the payload stage. The flight-test analysis of the measured signal attenuation is presented in reference 4.

The four-stage vehicle was designed to probe the region of high signal attenuation while flying an ascending trajectory so that it would exit the so-called "blackout region" after attaining peak speed. This type of trajectory was chosen rather than the trajectories used in the flight tests of reference 3, since under these conditions aerodynamic heating problems are minimized and the performance

of the instrumentation can be monitored before and after the period of expected high signal attenuation.

The fourth (payload) stage attained a maximum velocity of 17,800 feet per second at a burnout altitude of 175,000 feet. The flight test was conducted at the NASA Wallops Station, Wallops Island, Va.

SYMBOLS

a_l	longitudinal acceleration, g units
a_n	normal acceleration, g units
a_t	transverse acceleration, g units
M_α	pitching-moment-curve slope, rate of change of pitching moment for small angles of attack, ft-lb/rad
$C_{p,t}$	total pressure coefficient across a normal shock
I	pitch or yaw moment of inertia, slug-ft^2
I_X	roll moment of inertia, slug-ft^2
Δp	difference in pressure between diametrically opposed orifices, lb/sq in.
q	dynamic pressure, lb/sq ft
T	temperature
t	time, sec
η	angle of incidence, deg
ρ	density of air, slugs/cu ft

Subscripts:

XZ	reference plane of pressure orifices
∞	free stream

VEHICLE SYSTEM

General Arrangement

The vehicle used in the RAM A1 test was an unguided, four-stage, solid-propellant, aerodynamically stabilized rocket system. The first stage was a Castor XM33E3 motor with two auxiliary Recruit XM19 motors fastened on opposite sides between the Castor fins. The second and third stages were XM45 motors, and the fourth (payload) stage was a Recruit XM19 motor. The two auxiliary Recruit rockets, which had nozzles canted so that the thrust would be directed through the approximate center of gravity of the four-stage configuration, were used to provide additional acceleration for the first 2 seconds of flight to overcome the wind problem resulting from low initial acceleration. The overall length of this system was approximately 65 feet and the weight approximately 14,400 pounds at launch. A sketch including pertinent dimensions of the four-stage configuration is shown in figure 1. A photograph of the payload stage and booster system mounted on a zero-length boom-type launcher is shown in figure 2. Figure 3 shows the four-stage configuration just after launch. Figure 4 is an end view of the first stage and shows the attachment of the two auxiliary Recruits in relation to the first-stage fins.

The first three stages of the rocket system were stabilized by fins. The fins of the first and second stages were mounted in line and the fins of the third stage were interdigitated with those of the first and second stages. The second- and third-stage fins were canted 0.4° and 0.6°, respectively, to impart a rolling motion during certain times in the flight. The vehicle roll program is discussed in a subsequent section. Figure 5 is a photograph of the third-stage fin-shroud assembly and is typical of the second-stage fin-shroud assembly. The fourth stage had a 10° half-angle conical frustum stabilizing surface.

Stage Coupling and Separation Devices

A magnesium adapter bolted to the first-stage motor was coupled to the second-stage nozzle with a Marman band as shown in figures 6(a) and 6(b). The lips on the adapter and the nozzle were clamped together with segments held in place by the Marman band. Two of the four bolts holding the assembly together were explosive bolts. A conventional aircraft bolt was altered to have a deep thread relief and the inside was bored out and filled with approximately 2 grams of pistol powder. A timer-actuated zero-delay squib ignited the powder a short time after the burnout of the first-stage motor, destroyed the bolt, and permitted the first stage to drag separate. Figure 6(a) also shows a lock-key arrangement which was used to prevent in-flight rotation between the first and second stage.

The second and third stages were coupled with a threaded aluminum blowout diaphragm and locked (to prevent unscrewing) as shown in figures 6(c) and 6(d). The diaphragm was screwed into the third-stage nozzle; then the second-stage steel adapter was screwed tight on the diaphragm and into the matching lips and face of the third-stage nozzle. The second-stage adapter was then bolted to the thrust face of the second-stage motor. Ignition of the third stage caused the

diaphragm to collapse and free the third stage from the burned-out second-stage booster. In order to obtain a desired differential pressure for separation purposes, the slotted segments and web of the blowout diaphragm were covered with a fiber glass-rubber composite and bonded to the diaphragm as shown in figure 6(c).

The third and fourth stages were coupled and locked together in a manner similar to that used for the second and third stages as shown in figures 6(e) and 6(f). A threaded aluminum diaphragm was screwed into the fourth-stage flare and the third-stage steel adapter was screwed to the diaphragm so that tight contact was made with the face and lips of the fourth-stage flare. Then the entire fourth-stage motor, flare, and adapter combination was bolted to the face of the booster by using bolt holes in the adapter. The ignition of the fourth stage caused the diaphragm to collapse and free the fourth stage from the third-stage booster. The blowout diaphragm used in the third- to fourth-stage adapter was covered in the manner previously described for the second- to third-stage blowout diaphragm.

Payload Stage

Since the payload tested in the present investigation was attached to the front end of the fourth stage and also underwent the high-speed portion of the flight test, details of its structure and instrumentation are presented.

The payload stage was a body of revolution, approximately 147 inches long, with a hemispherically blunted 9° half-angle conical nose, a cylindrical midsection, and a 10° half-angle flare section at the rear. Figure 7(a) shows dimensions of the payload stage and some details of the nose on which skin temperature and vehicle angle-of-attack measurements were made. A photograph of the payload stage is shown in figure 7(b).

The test nose cone of the payload stage consisted of a 1-inch-radius hemispherical apex on a 9° half-angle conical section. The hemispherical apex was machined from a solid block of high-conductivity, electrolytic-pitch copper and was threaded to the cone which was chemically milled from 0.125-inch-thick Inconel to a nominal 0.095-inch thickness and then rolled and seam welded. The copper and Inconel surfaces were finished with fine-grit polishing compound with only a moderate effort made to attain a low-roughness finish. Figure 8(a) shows the dimensions of the test nose and the location of the thermocouples and the differential pressure orifices. Also noted on this figure is the measured skin thickness at each temperature measuring station. A photograph of the test nose is shown as figure 8(b).

The cylindrical section just behind the nose cone was of double-wall construction. The inner wall and main structural member was a cylindrical magnesium section; this section, bolted to the thrust face of the Recruit motor, housed the telemeter equipment and protected it from external radiation. The outer heat shield (nonstructural) was spun from 0.05-inch-thick Inconel and was free to expand rearward.

The flare, which provided aerodynamic stability for the payload stage, was constructed of 0.078-inch-thick Inconel and was attached to the rear face of the payload-stage rocket motor.

General Vehicle Mass Properties

Time histories of the vehicle weight, center-of-gravity locations, and yaw, pitch, and roll moments of inertia are presented in figure 9 for the four stages of the flight configuration. These data are based on both calculated and measured mass properties of the rocket motors, fin-shroud assemblies, adapter sections, components, and vehicle payload. Actual measurements obtained included the mass properties of the payload stage and the weights and center-of-gravity locations of the individually loaded first-, second-, and third-stage assemblies. The fin-shroud assemblies of the first three stages and the three adapter sections between the stages were also weighed. A lack of suitable swing facilities precluded actual measurement of the inertia properties of the first three stages.

Protection From Aerodynamic Heating

The surfaces of the four-stage vehicle were analyzed to determine the areas that would experience severe aerodynamic heating. Critical areas were covered with thermal-protection materials.

The first-stage magnesium fin (fabricated from 0.25-inch-thick plate) had leading-edge wedges covered with 0.010-inch-thick fiber glass and then capped with a sheet of 0.032-inch-thick Inconel. The second- and third-stage magnesium fins (fabricated from 0.188-inch-thick plate) were completely covered with thermal-protection materials. The leading-edge wedges and flat sections were covered with 0.018-inch-thick fiber glass and then covered with 0.032-inch-thick Inconel sheet. The leading edge of the second-stage fin had an additional cap, of 0.06-inch-thick Inconel, which extended about 1.5 inches back from the leading edge. The third-stage fin also had an additional stainless-steel cap which extended back from the leading edge approximately 2 inches. This cap was machined to 0.25 inch flat across the leading edge (to reduce the stagnation-line heat transfer) and was 0.70 inch deep. The trailing-edge wedge sections of the second- and third-stage fins were sprayed with a high-temperature paint to a thickness of 0.03 inch. Figure 10 shows photographs of the heat-protection material on the leading edges, the leading-edge wedges, and flat sections of the second- and third-stage fins.

The first-stage adapter was protected from aerodynamic heating with a high-temperature paint, sprayed on to a thickness of 0.065 inch.

The calculated temperature rise for the cylindrical section of the fourth-stage motor indicated that the liner between the motor-case wall and the grain could become soft and, under acceleration loads, the motor grain would slump. Thus, the fourth-stage-case wall was thermally protected with a high-temperature ablative paint sprayed on to a nominal thickness of 0.03 inch. As an added measure of conservatism, the holes in the front and rear end of the fourth-stage

motor (see fig. 7(a)) were filled completely with asbestos material and the sta-
bilizing flare of this stage was sprayed with a high-temperature ablative paint
to a thickness of 0.020 inch.

INSTRUMENTATION

Vehicle

The telemeter, carried in the forward part of the payload stage, transmitted
seven continuous channels of information. These were normal and transverse accel-
erations, thrust and drag accelerations, skin temperature, differential pressure
measurements, and antenna efficiency (forward power, reflected power, and imped-
ance) measurements. The antenna-efficiency measurements, which were the primary
purpose of this flight test, are presented with analysis in reference 4.

Readings from 12 thermocouples were commutated on the temperature channel
and these data were recorded approximately every 0.2 second. The locations of the
12 thermocouple stations are shown in figure 8(a). The nine thermocouples
installed on the Inconel conical section of the test nose were spot welded to the
inner surface of the skin. The remaining three thermocouples installed in the
copper apex were silver soldered. Three holes were drilled in the copper apex to
the required depth and the thermocouples were placed in the holes until they
bottomed and then a common sweating process was used to complete the installation.

Thrust and drag accelerations were measured by accelerometers calibrated in
gravitational units from -5g to 180g of thrust and from 2g to -5g of drag. Normal
and transverse accelerations were measured continuously by accelerometers cali-
brated to ±15g. The normal and transverse accelerometers were employed to deter-
mine flight irregularities during the boost portion of the flight.

The pressure orifices, located on the hemispherical surface of the nose cone
and shown in figure 8(a), were connected to a differential pressure cell for use
as an angle-of-attack indicator. The differential pressure cell was calibrated
to a full-scale range of 1.5 to -1.5 pounds per square inch and capable of
100-percent overload without affecting its linearity.

A radio beacon, located in the telemeter section of the payload stage, used
the slot antenna which is shown in figure 8(a). The efficiency of the slot
antenna was determined from measurements made on the transmission line feeding
the slot. This information was transmitted to ground receiving stations through
the telemeter antenna located on the cylindrical portion of the payload stage as
shown in figure 7(a). The results of these measurements are shown and discussed
in reference 4.

Vehicle roll rate was obtained from the variation in signal strengths, from
the onboard transmitters, measured at the various ground receiving stations. As
the vehicle made one complete revolution, two null points were noted in the sig-
nal intensity trace. These null points corresponded to those in the preflight
check of the radiation pattern for the vehicle antenna arrangement.

6

Ground Range

Telemetry receiving stations were located at the launching site (Wallops Station) and on a Wallops Station sea-range telemeter trailer located on a ship due east and approximately 95 miles down range from the launching site. Radio signal strength from the transmitters onboard the payload stage were monitored at Wallops Station, on the down-range ship, at Langley Station, and at Coquina Beach, N.C.

The payload stage was tracked by FPS-16, Reeves Mod. II SCR-584, and SCR-584 space-position radar sets to provide velocity and trajectory data in addition to the data provided by the instrumentation carried internally. Atmospheric and wind conditions were determined by means of a radiosonde launched near the time of flight and tracked by a Rawin set AN/GMD-1A to an altitude of approximately 85,000 feet. In an attempt to obtain atmospheric data for the high-altitude portion of the flight, an Arcasonde and an Arcas-Robin were launched soon after the flight of the test vehicle and tracked by the FPS-16 radar set. Atmospheric density and temperature data were obtained at altitudes from 130,000 feet to approximately 185,000 feet.

Accuracy

The measured temperatures are believed to be accurate within ±1 percent of the full-scale range of the thermocouple instrumentation. Therefore, the skin temperature measurements are accurate within ±20° F.

The differential pressure measurements are believed to be accurate within ±2 percent of the calibrated full-scale range of the differential pressure cell. This results in an accuracy in Δp of ±0.06 pound per square inch. The angles of incidence of the payload stage, calculated from the measured differential pressure data, are believed to be accurate within ±1.0°.

The velocity data which were obtained by differentiation of the data from the FPS-16 space-position radar and by integration of accelerometer data are believed to be accurate within ±100 feet per second.

FLIGHT-TEST RESULTS AND DISCUSSION

Trajectory Flight Plan and Test Conditions

The four-stage rocket configuration was launched at 70° elevation and boosted along a ballistic trajectory to an altitude of approximately 80,000 feet with the Castor motor. The remaining three stages were fired in rapid sequence on an ascending trajectory to obtain maximum velocity at as low an altitude as possible without exceeding allowable skin temperatures.

The two Recruit motors, which burned only 1.9 seconds, were added to the first stage to increase the take-off acceleration of the 14,400-pound combination

from about 3.8g (without Recruits) to about 10g. The increase in take-off g units was necessary so that at low altitudes (up to 400 feet) dispersion due to wind effects would be minimized.

The two Recruit motors were fired by means of pull-away clips when the combination began to move so that they would not ignite prior to the Castor motor ignition. Also, with this firing sequence the Castor motor was pressurized and therefore strengthened before the thrust of the Recruits was applied to the structure.

At 38.6 seconds after launch, the Castor motor drag separated when zero-delay squibs, ignited by a preset mechanical timer which was actuated by an inertia switch at launching, fired two explosive bolts to release the Marman band arrangement. The remaining stages coasted to an altitude of approximately 80,000 feet at which time the second switch on the preset mechanical timer closed and the instantaneous initiators fired the pyrogen unit located in the head cap of the second stage and thereby ignited the second stage. The third and fourth stages were fired automatically at burnout of the previous stage by means of pressure switches cocked and tripped by the rise and fall, respectively, of the chamber pressure of the motor of the previous stage.

As noted in figure 1, the second- and third-stage fins were canted counterclockwise (viewed from the rear) 0.4° and 0.6°, respectively. This canting imparted sufficient rolling motion to the last three stages of the system to avoid a potential roll-resonance condition (coupling of roll and short-period frequency) during this portion of the flight trajectory. This roll was also necessary to minimize the dispersion of the fourth stage which operated at high altitudes (low q region). The vehicle roll requirements are discussed in more detail in the section entitled "Roll Rates."

A portion of the flight trajectory followed by the four-stage system is shown in figure 11. Times of significant events are indicated on the trajectory. The time histories of the free-stream test conditions of velocity and altitude are shown in figure 12.

Trajectory data presented for the flight tests are based mainly on the results obtained from the RCA AN/FPS-16 tracking radar. Altitude, horizontal range, and velocity of the vehicle were derived from FPS-16 radar data which were recorded numerically and used in conjunction with an IBM 650 digital computer programed for an oblate earth. All reduced radar data were converted to the launch-site reference. Data furnished by supporting radar units were reduced similarly for comparative purposes. The velocity data obtained from both the FPS-16 and SCR-584 radars were corrected for winds as measured by radiosonde instrumentation. During the thrusting of the third and fourth stages, velocity was also determined (for comparative purposes) from integration of the telemetered longitudinal accelerations.

Vehicle Environmental Conditions

Time histories of free-stream Mach number and Reynolds number per foot are shown in figure 13(a). Figure 13(b) shows the free-stream flight variation of dynamic pressure. These quantities were calculated for altitudes up to approximately 85,000 feet ($t \approx 44$ seconds) by using atmospheric data furnished by radiosonde. For altitudes greater than 85,000 feet, the ARDC 1959 model atmosphere of reference 5 was assumed and used directly, since measured atmospheric data at the higher altitudes were obtained only for a limited portion of the payload-stage environment and some question exists as to their degree of reliability.

A comparison of the measured density and temperature data with the ARDC 1959 model atmosphere is shown in figures 14(a) and 14(b). In figure 14(a) the density measurements obtained from the radiosonde and Arcas-Robin are in good agreement with the ARDC 1959 model atmosphere, however, the agreement with the Arcas-Robin data may be fortuitous. The temperature measurements obtained by radiosonde and Arcasonde are also in good agreement with the model atmosphere as shown in figure 14(b).

Accelerations

Figure 15 shows the time histories of the measured accelerations of the four-stage vehicle, uncorrected for off-the-center-of-gravity locations. The longitudinal accelerometer was included in the vehicle instrumentation as an added means for velocity determination in case of radar malfunction and also as a means for monitoring actual stage ignition and burnout times. The maximum longitudinal acceleration attained by the payload stage was approximately 144g and is shown in figure 15(a). Measurements made by the normal and transverse accelerometers, intended for monitoring gross vehicle motions, are shown in figure 15(b). These measured accelerations were less than 1 g during the motor burning times; however, at ignition times an increase occurred which was probably due to the initial separation disturbance. The very small trim accelerations recorded throughout the flight indicated that the various stages were well balanced dynamically and structural misalinements were small.

Roll Rates

The flight time histories of the measured roll rates and calculated short-period (pitch) and first-mode structural frequencies of the four-stage configuration are shown in figure 16. This figure illustrates two of the varied aerodynamic and structural problems which required solutions. The aerodynamic problem is that of roll-pitch resonance. This is a condition in which motions about the flight path are amplified to a large extent when the rolling frequency becomes equal to the nutational frequency. This resonant frequency $\sqrt{\dfrac{M_\alpha}{I_X - I}}$ is very nearly equal to the model nonrolling natural pitch frequency $\sqrt{-\dfrac{M_\alpha}{I}}$ for the slender configuration under consideration.

In the present test, the first-stage fins of the vehicle system were set for zero roll; however, manufacturing tolerances were such that a small residual cant or twist existed. The measured first-stage roll frequency shown in figure 16 results from this small ($< 0.1^{\circ}$) cant. As can be seen, there is an adequate margin between the roll and pitch frequencies. Since the latter stages operate at high altitude, dynamic pressure is low and, therefore, the short-period pitch frequency is fairly low for these stages; in fact, fin incidence angles due to manufacturing tolerances would be very likely to produce a roll rate very close to pitch frequencies. Therefore, fairly large angles of incidence, 0.4° and 0.6°, were intentionally put into the second- and third-stage fins, respectively, so that the roll rate would rapidly pass through the pitch frequency. Therefore, the angular deviation of the vehicle from the flight path was kept small by passing through the resonant frequency relatively quickly.

Some aerodynamic instability was expected at the time of the fourth-stage operation because rocket-motor exhausts at high altitudes (low density) can cause extensive separation of the flow over the vehicle; this flow separation can substantially reduce the effectiveness of the stabilizing surface (ref. 6). In view of the mission requirements and dispersion limitations of the impact area of the payload stage, it was necessary to determine the roll rate required to restrain the maximum total yaw angles of the fourth stage to about 5°. Therefore, estimated maximum total yaw angles and rates at fourth-stage separation, thrust asymmetry, and a reduction in flare effectiveness at small angles of attack for the fourth stage were incorporated into the equations of motion and were numerically solved with the IBM 7090 electronic data processing system. Results of this simulation showed that a roll rate of approximately 4 cycles per second was necessary to maintain the angular deviation of the geometric longitudinal axis from the flight path within 5° during the data-gathering period (midway through burning and approximately 6 seconds after burnout) of the fourth stage. Figure 16 shows that the roll rate at ignition of the fourth stage was approximately 4.5 cycles per second and increased to approximately 4.75 cycles per second at burnout. This increase in the roll rate for symmetrical bodies of revolution without fins has been measured in other flight tests. Roll amplification has also been measured during the thrusting of 10-inch-diameter spherical rocket motors and is discussed in reference 7.

The rolling of a large missile at high rates presents some structural problems and the limit of this roll is determined for the most part by the structural characteristics. The roll rate during the operating time of the second and third stages could not be increased to too high a rate or it would approach the first-mode structural frequency and again an undesirable resonant condition could occur. The first-mode structural natural frequencies for the RAM A1 vehicle, shown in figure 16, were calculated by the method of reference 8.

Angle of Attack

The difference in pressures between diametrically opposed orifices located in the hemispherical apex of the payload stage was measured over the range of the test trajectory. Figure 17 shows the time variation of the measured differential pressures. The orifices were located in the hemispherical apex on 45° radius

vectors measured from the vehicle longitudinal axis. (See fig. 8(a).) This measurement was included in the instrumentation of the payload stage so that a determination of the flow angularity during the high-speed portion of the test (thrust and coast) period of the payload stage could be made.

Wind-tunnel tests on cones (ref. 9) and unpublished data on hemispherical noses have shown that differential pressure measurements on the nose can be used for determining flow angularity at hypersonic speeds. In order to determine angle of attack accurately with this technique, differential pressure measurements in two orthogonal planes would be required for a rolling missile. For the present test, differential pressure measurements were taken in one plane on the premise that the rolling motions would be well above resonance and the resulting angular epicycloid motions would be nearly circular (ref. 10). In this case, incidence-angle measurements in one rotating plane would provide a close approximation of the vehicle angle of attack. Reference 9 shows that Newtonian theory may be employed to determine the incidence angle. With the differential pressure measurements in the XZ-plane (the test case) and the pressure orifices inclined 45° from the axis of symmetry, η_{XZ} of the rotating plane may be determined from the following expression:

$$\frac{1}{2} \sin^{-1}\left[\frac{\Delta p_{XZ}(144)}{q_\infty C_{p,t}}\right] = \eta_{XZ} \tag{1}$$

At Mach numbers greater than 10, $C_{p,t}$ is approximately equal to 1.84 and constant.

The time history of η_{XZ} during the thrust and coast of the payload stage is shown in figures 18(a) and 18(b). Simulation studies of the vehicle motions in this flight regime show that the η_{XZ} time histories of figure 18 may be expected to result from epicycloid motions which are nearly circular. The studies also showed that the maximum points of the envelope were approximately equal to the maximum angle of attack of the rolling vehicle.

The symmetry of the flight time histories of η_{XZ} shown in figure 18 also indicates that the roll axis was alined with the payload-stage geometric axis and that the trim angle in the plane of the measurements was negligible. The maximum angle of attack was about 6° during the payload-stage thrust period and about 4° during the subsequent coast flight.

Skin Temperatures

Time histories of skin temperatures measured at various stations on the nose cone of the payload stage during the flight are shown in figure 19. Thermocouple stations 1, 2, and 3 were located in the solid copper hemispherical apex of the nose cone. Station 1, located at the stagnation point, reached a higher temperature than station 2 or station 3 (the coolest station) located further downstream.

Station 4, located on the Inconel nose cone just aft of the copper-Inconel juncture, shows a peak temperature of about 650° F which is lower than that for the remainder of the stations located on the Inconel cone. This lower temperature at station 4 is probably due to its proximity to the thick copper apex. Stations 5 to 12, located on the Inconel nose, all reached a maximum of approximately 700° F. During the period of approximately 66 to 70 seconds, no temperature data are available since the temperature channel of the telemetry was noisy and no interpretation of the data could be made.

The measurements presented in figure 19 are average temperatures of a rolling vehicle at oscillatory angles of attack. Temperature measurements at stations 5 and 9, which are diametrically opposite, and stations 7 and 10, similarly located, indicate that a temperature averaging process did occur for this rolling case although the vehicle oscillated at angles of attack.

CONCLUDING REMARKS

A general description, some details of mechanical design and construction, and flight performance of a four-stage solid-propellant rocket vehicle have been presented. The vehicle was designed for the purpose of investigating the effect of ionization on radio-signal attenuation during reentry flight.

The vehicle was designed to probe the region of high signal attenuation while flying an ascending trajectory so that it would exit the so-called "blackout region" after attaining peak speed. Under these conditions aerodynamic heating problems were minimized and the performance of the instrumentation was monitored before and after the period of high signal attenuation.

The vehicle successfully followed the planned trajectory and achieved a velocity of 17,800 feet per second at an altitude of 175,000 feet.

The performance data discussed included the velocity and altitude, accelerations, and roll rates of the multistage vehicle system. Angle-of-attack data for the rolling fourth (payload) stage and also temperature data on the nose cone were also discussed.

Langley Research Center,
     National Aeronautics and Space Administration,
          Langley Station, Hampton, Va., November 30, 1962.

REFERENCES

1. Huber, Paul W., and Gooderum, Paul B.: (With Appendix A by Theo E. Sims and Duncan E. McIver, Jr., and Appendix B by Joseph Burlock and William L. Grantham): Experiments With Plasmas Produced by Potassium-Seeded Cyanogen Oxygen Flames for Study of Radio Transmission at Simulated Reentry Vehicle Plasma Conditions. NASA TN D-627, 1961.

2. Ellis, Macon C., Jr., and Huber, Paul W.: Radio Transmission Through the Plasma Sheath Around a Lifting Reentry Vehicle. NASA TN D-507, 1961.

3. Graves, George B., Jr., and Markley, J. Thomas: Telemeter Transmission at 219.5 Megacycles From Two Rocket-Powered Models at Mach Numbers up to 15.7. NACA RM L58D18a, 1958.

4. Sims, Theo E., and Jones, Robert F.: Flight Measurements of VHF Signal Attenuation and Antenna Impedance for the RAM A1 Slender Probe at Velocities up to 17,800 Feet per Second. NASA TM X-760, 1963.

5. Minzner, R. A., Champion, K. S. W., and Pond, H. L.: The ARDC Model Atmosphere, 1959. Air Force Surveys in Geophysics No. 115 (AFCRC-TR-59-267), Air Force Cambridge Res. Center, Aug. 1959.

6. Falanga, Ralph A., Hinson, William F., and Crawford, Davis H.: Exploratory Tests of the Effects of Jet Plumes on the Flow Over Cone-Cylinder-Flare Bodies. NASA TN D-1000, 1962.

7. Martz, C. William, and Swain, Robert L.: Experimental and Analytical Study of Rolling-Velocity Amplification During the Thrusting Process for Two 10-Inch-Diameter Spherical Rocket Motors in Free Flight. NASA TM X-75, 1959.

8. Alley, Vernon L., Jr., and Gerringer, A. Harper: A Matrix Method for the Determination of the Natural Vibrations of Free-Free Unsymmetrical Beams With Application to Launch Vehicles. NASA TN D-1247, 1962.

9. Swalley, Frank E.: Measurement of Flow Angularity at Supersonic and Hypersonic Speeds With the Use of a Conical Probe. NASA TN D-959, 1961.

10. Nelson, Robert L.: The Motions of Rolling Symmetrical Missiles Referred to a Body-Axis System. NACA TN 3737, 1956.
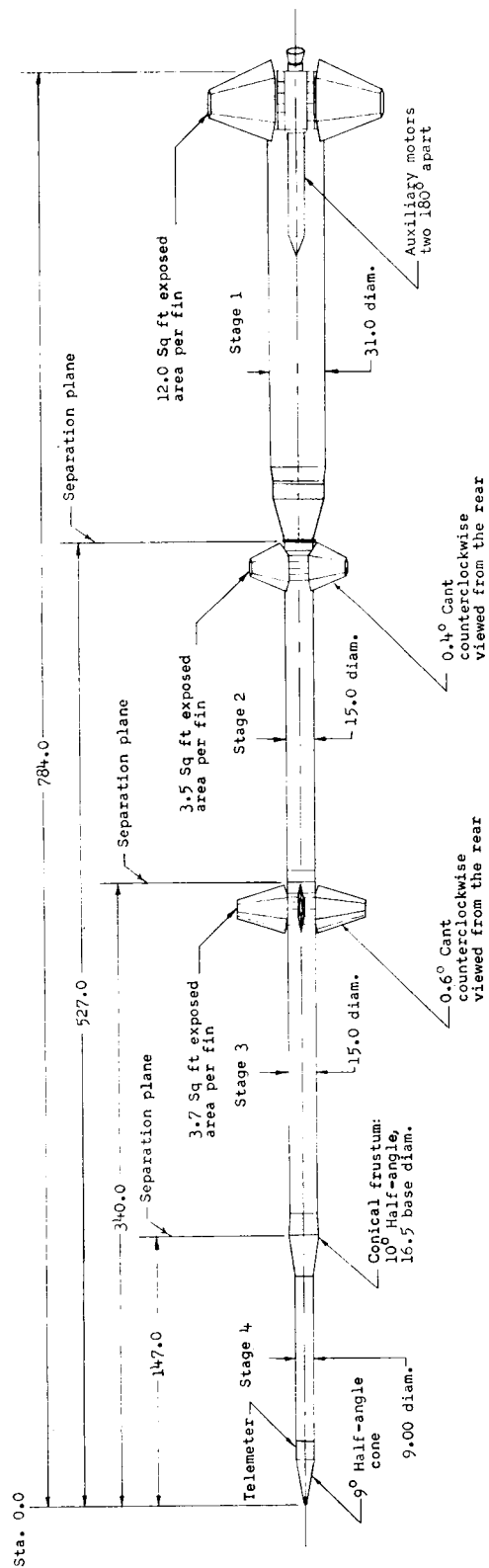
Figure 1.- Sketch of four-stage solid-propellant rocket system. All dimensions are shown only to the nearest tenth of an inch. Total launch weight, approximately 14,400 pounds.
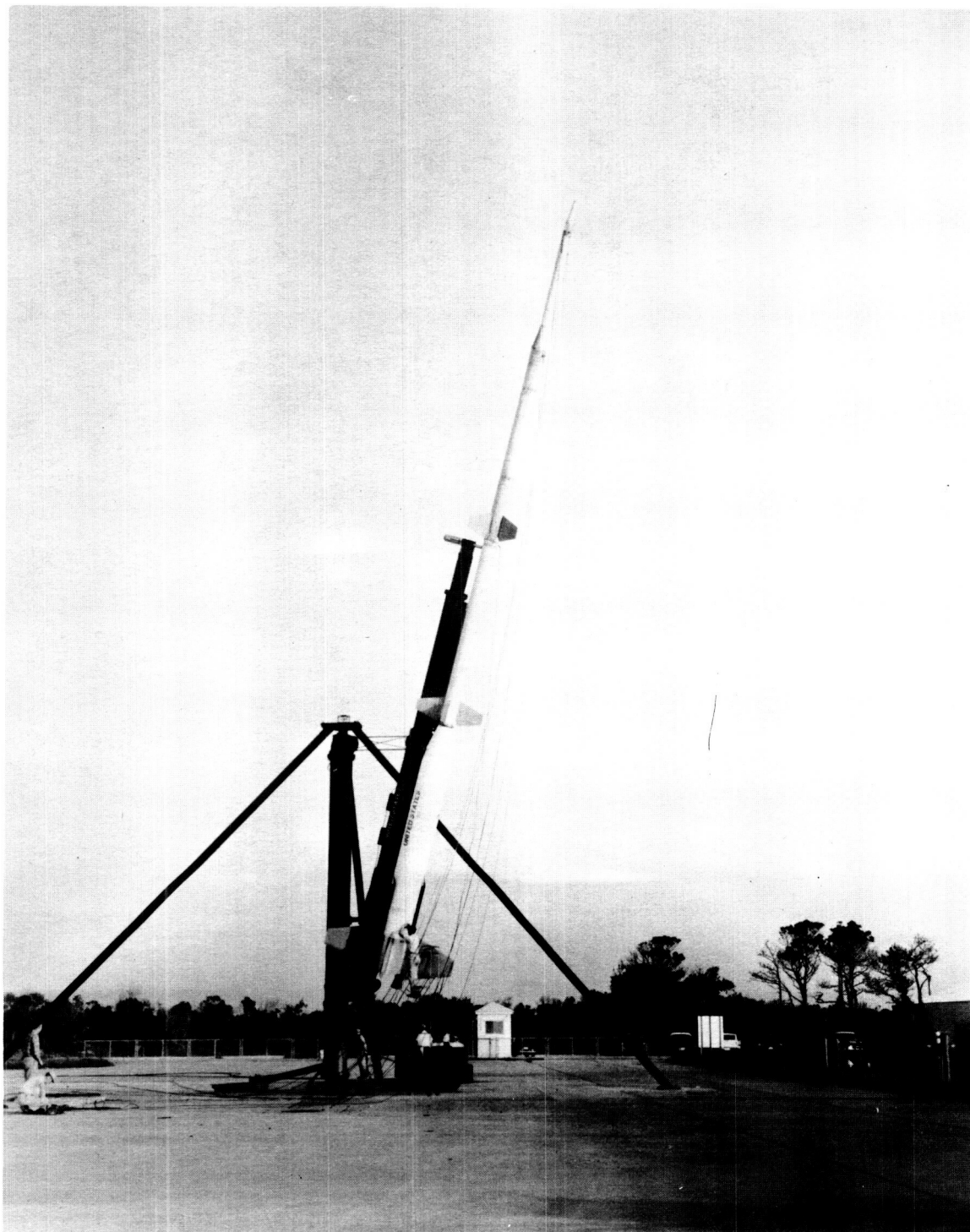
Figure 2.- Photograph of payload stage and booster system in launch position.   L-61-6238
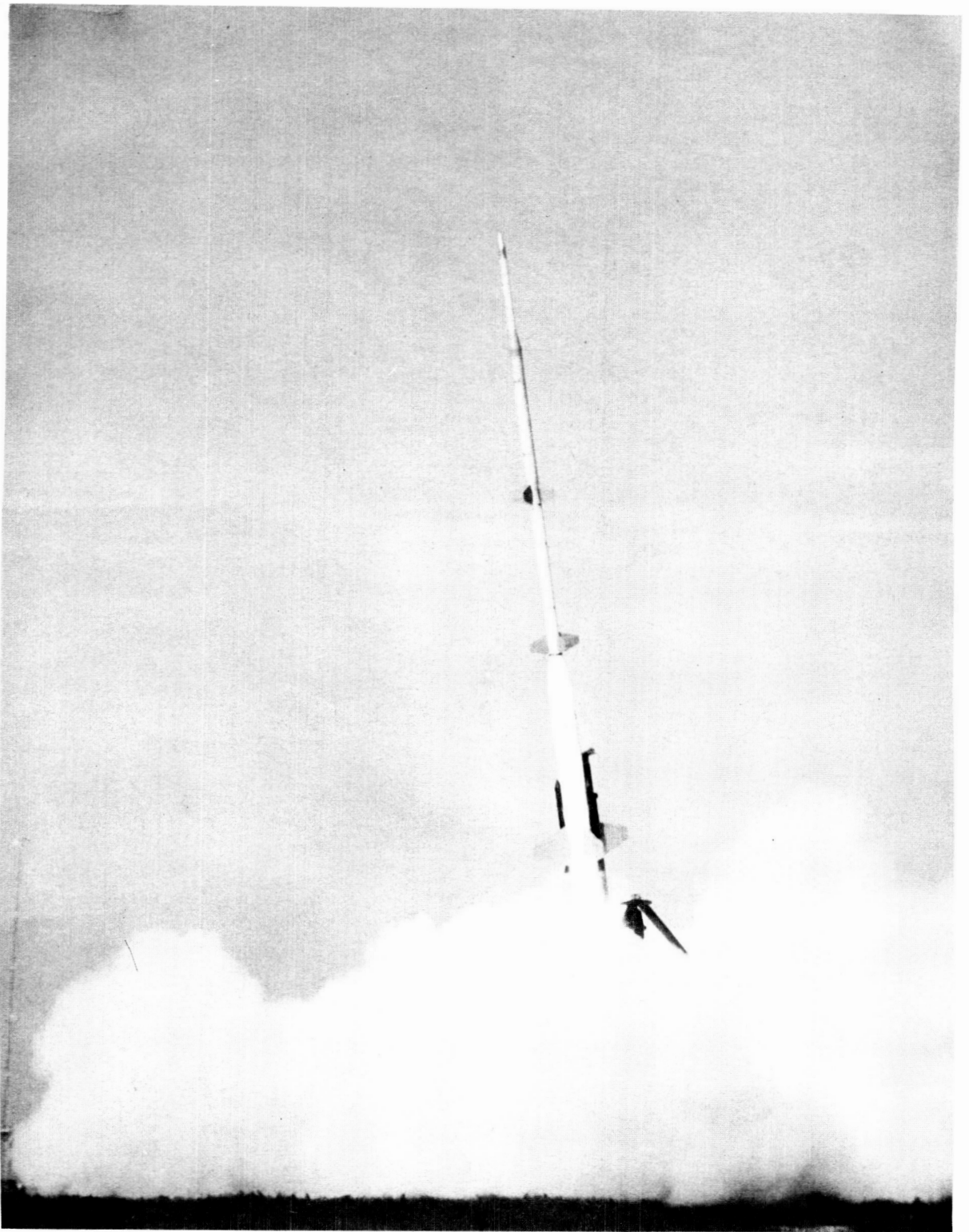
Figure 3.- Photograph of payload stage and booster system just after launch. L-61-6235

16

L-62-1435.1

Figure 4.- End view of first stage showing two auxiliary Recruit motors attached to fin-shroud assembly.
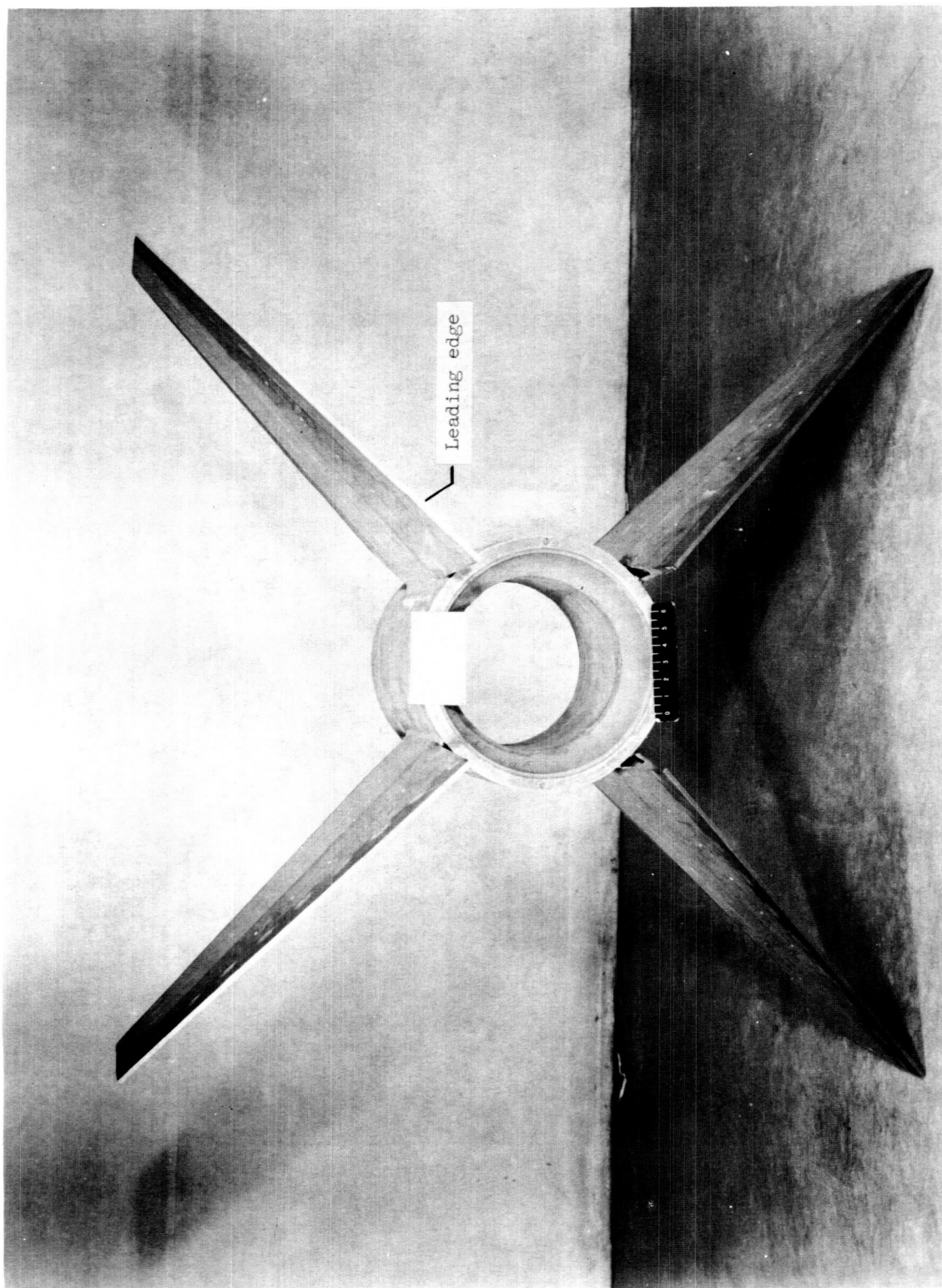
Figure 5.- Photograph of third-stage fin-shroud assembly. L-61-3151.1

Leading edge

Marman band

Pistol powder

Explosive bolt

Section A - A

Adapter

Explosive bolt
assembly

Squib leads

2nd Stage fin

Clamp segment

Nozzle stakes

Nozzle

Lock keys
two 180° apart

Shroud

A

A
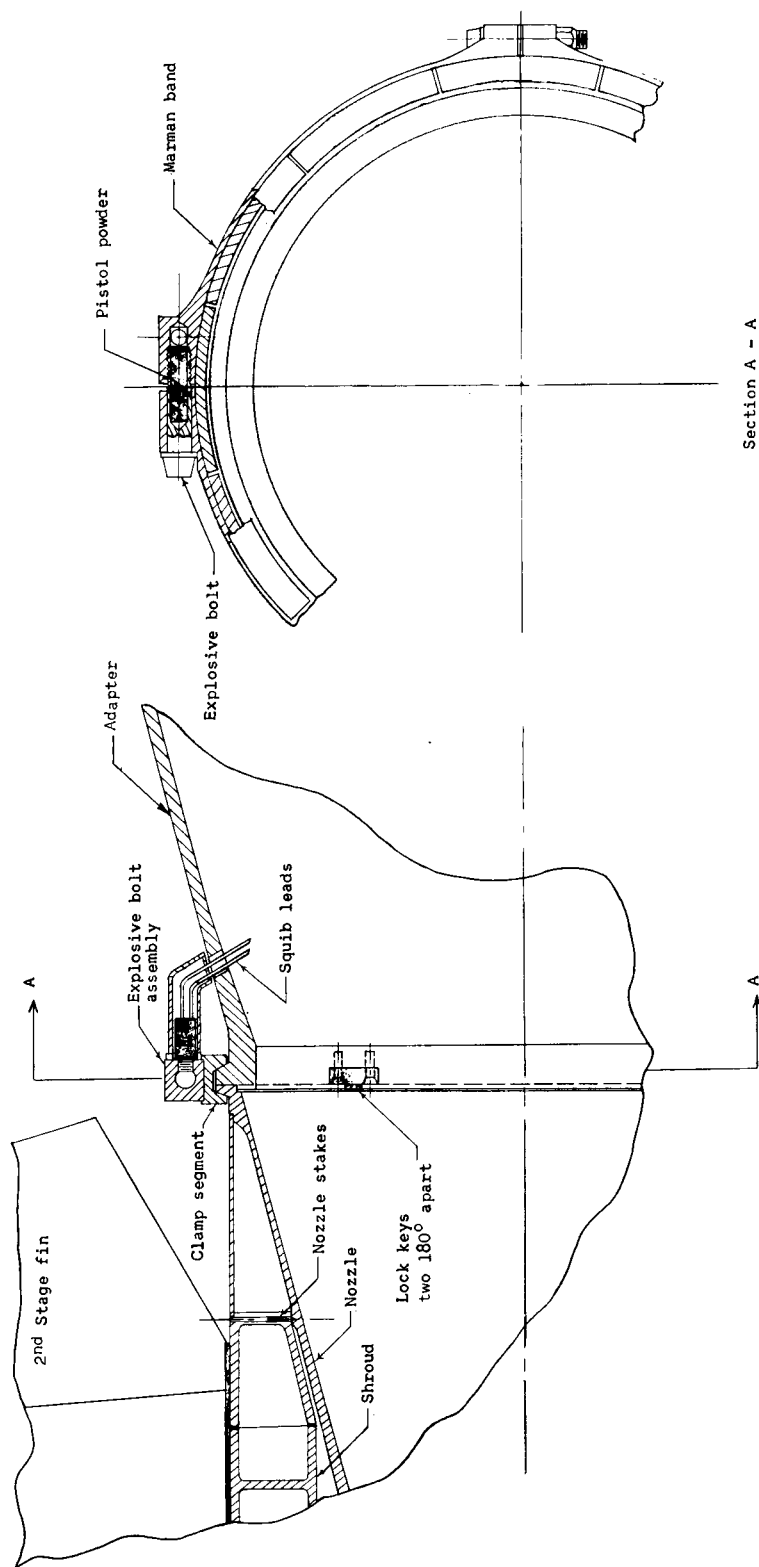
(a) First- to second-stage assembly.

Figure 6.- Coupling and locking devices between stages of four-stage system.

19
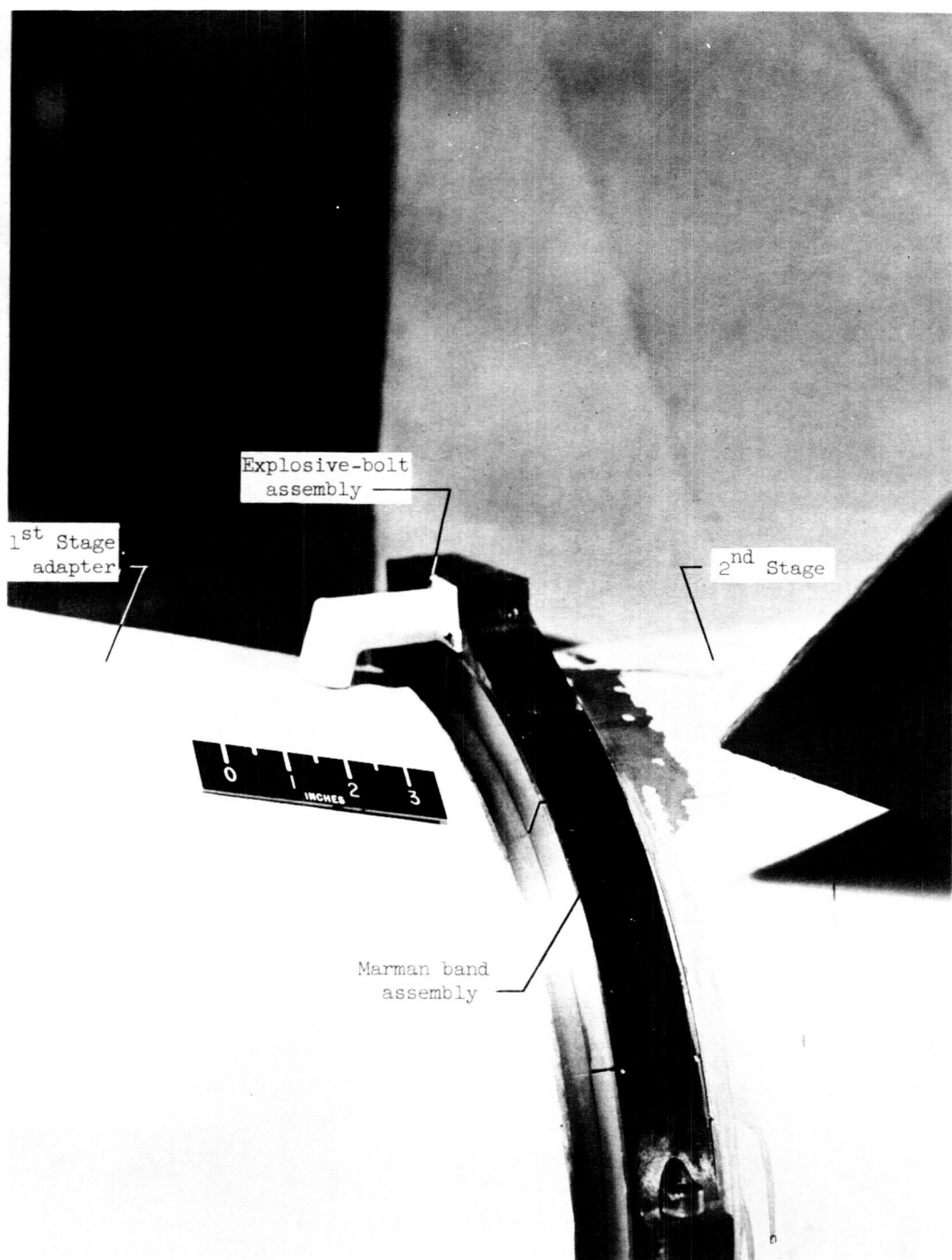
(b) Photograph of first- to second-stage assembly.   L-61-6243.1

Figure 6.- Continued.

Threaded flange

Slots

Slots and web covered with fiber-glass—rubber composite

Section A - A

Thin web

Adapter

Nozzle

Detail of lock assembly

Shroud

(c) Second- to third-stage assembly.

Figure 6.- Continued.

3rd Stage fins

Nozzle stakes

Nozzle

Shroud

Blowout diaphragm

Adapter

Fiber-glass—rubber composite

Lock assembly two 180° apart

A

A

3rd Stage fin-shroud assembly

Adapter

Blowout diaphragm

Lock assembly

Timer
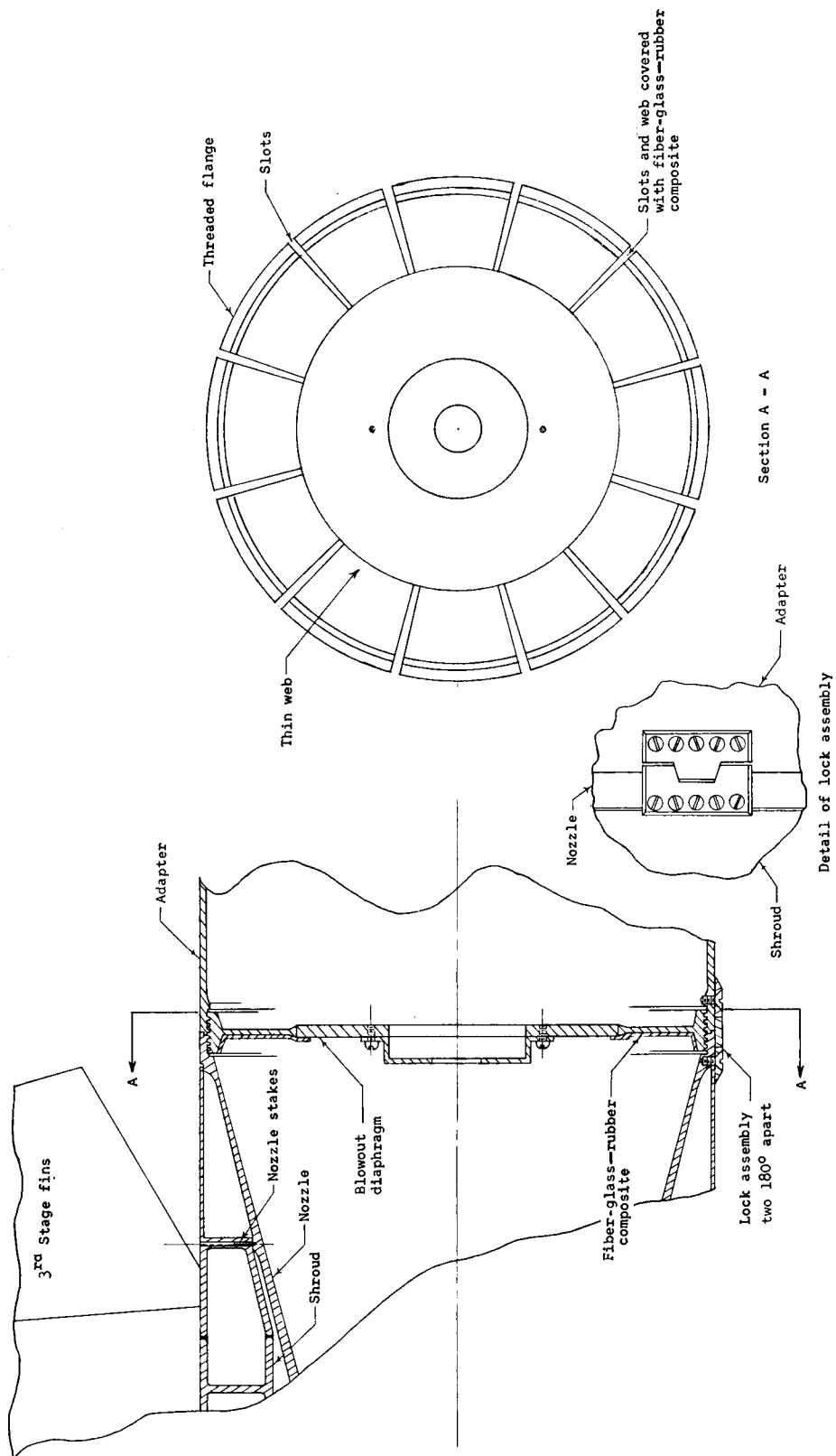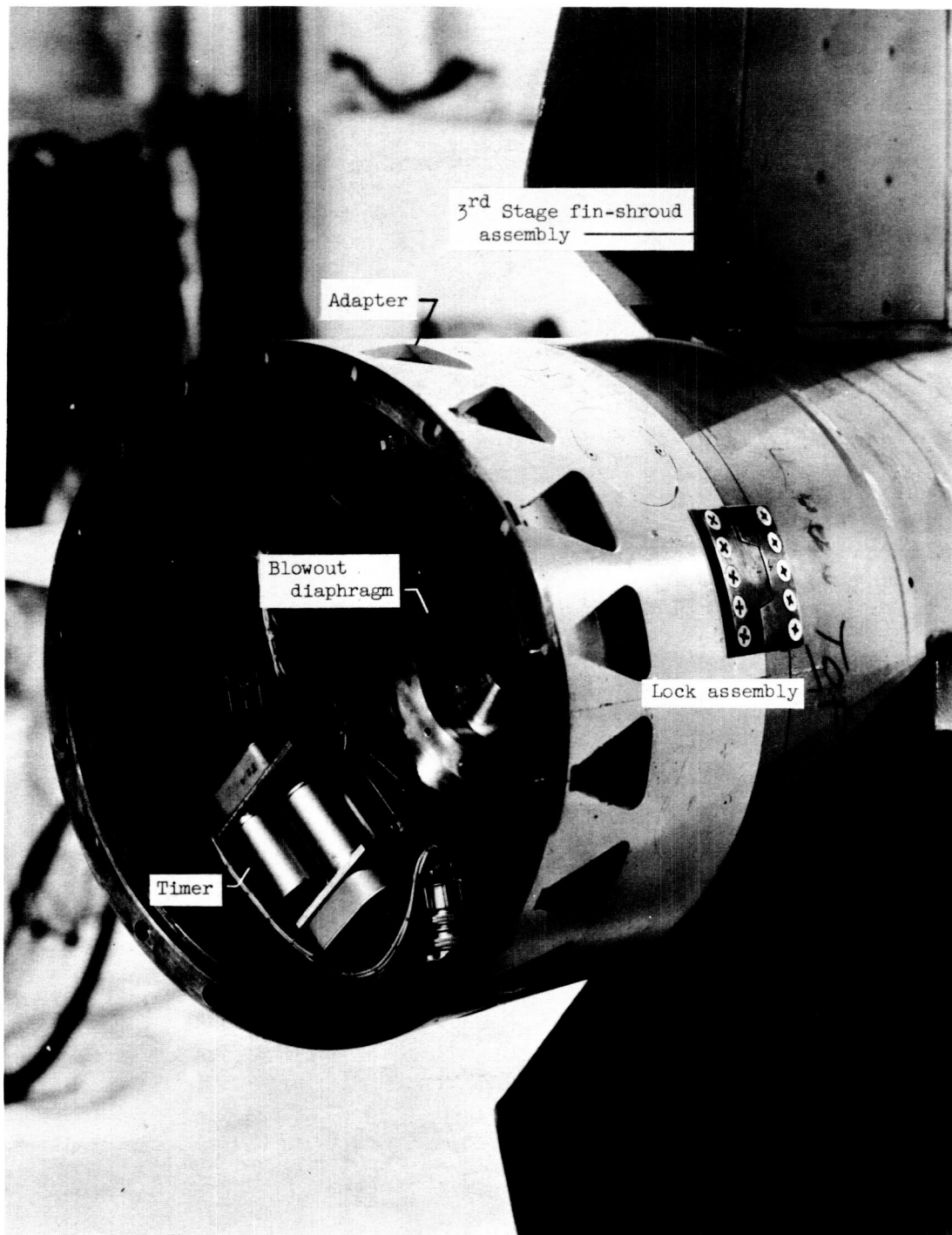
(d) Photograph of second- to third-stage assembly.   L-62-1429.1

Figure 6.- Continued.

Threaded flange

Thin web

Slots and web covered
with fiber-glass—rubber
composite

Section A - A

Adapter

Blowout
diaphragm

4th Stage flare

Nozzle

Fiber-glass—rubber
composite

Igniter lead
holder assembly

Lock assembly
two 180° apart

A

A
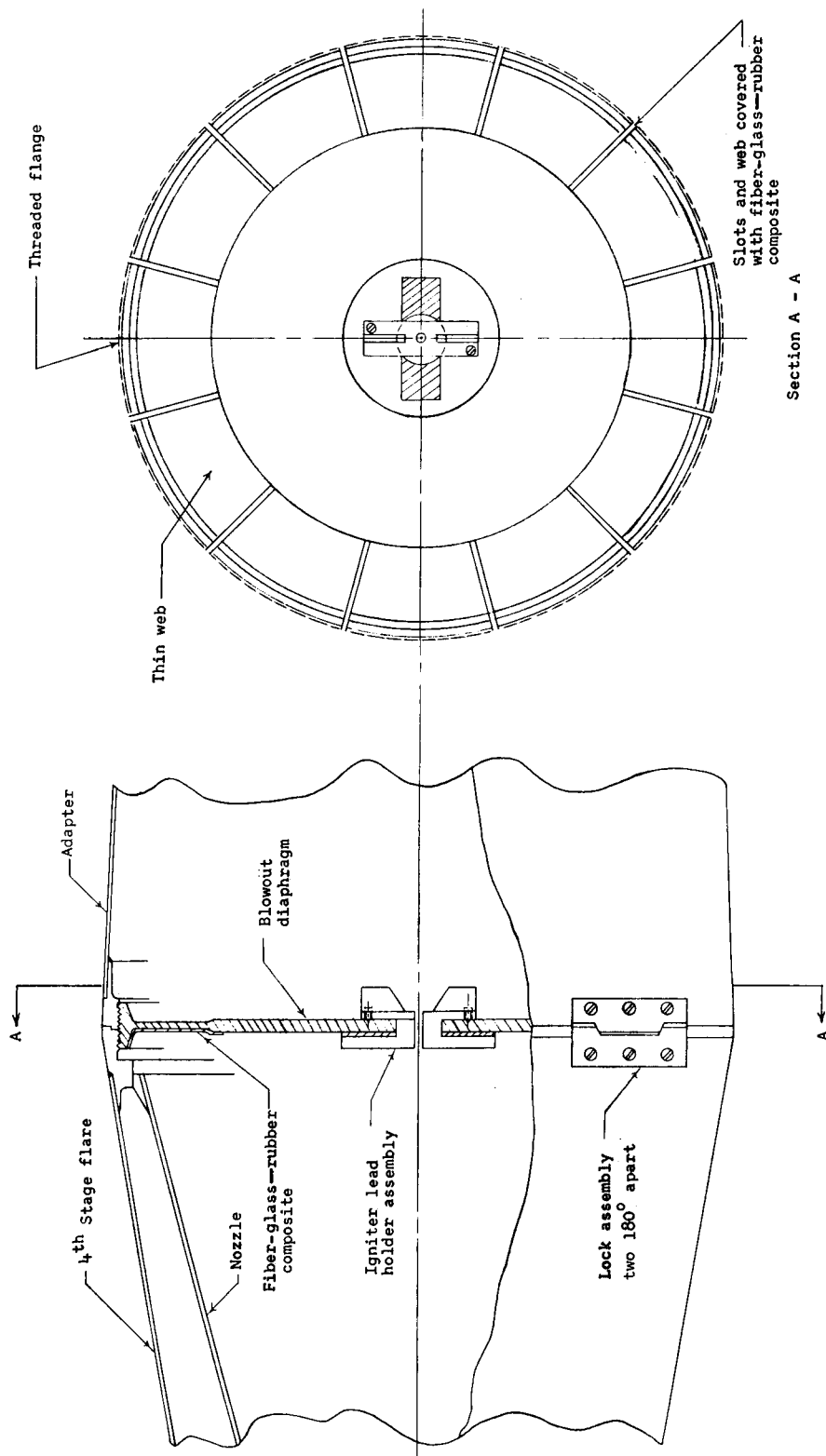
(e) Third- to fourth-stage assembly.

Figure 6.- Continued.

23

High-temperature
ablative paint

4th Stage flare

Lock assembly

INCH

4th Stage adapter
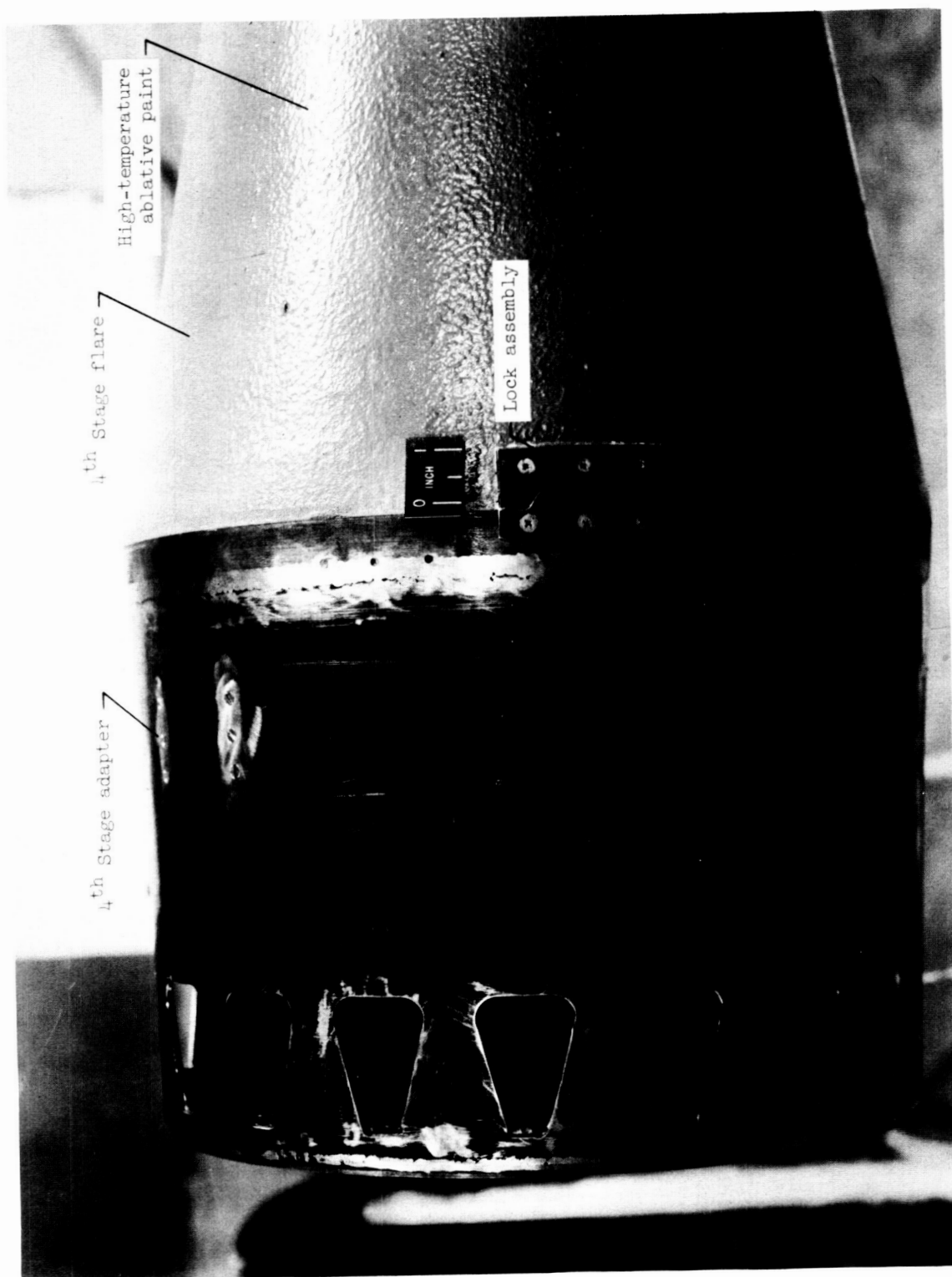
(f) Photograph of third- to fourth-stage assembly. L-62-1431.1

Figure 6.- Concluded.

Wall thickness

Nose tip   4.0   copper
Conical section of nose   0.095 Inconel
Telemeter heat shield   0.05   Inconel
Stabilizing flare   0.078 Inconel

• Loaded c.g., 78.51 inches from nose

x Burned out c.g., 77.99 inches from nose

16.50 diam.

10° Half-angle flare

9.00 diam.

146.97

125.51

Lightening holes

Telemeter antenna

Telemeter section

35.60

23.10

Radio beacon antenna

9° Half-angle cone

1.00 rad.

Sta. 0.0
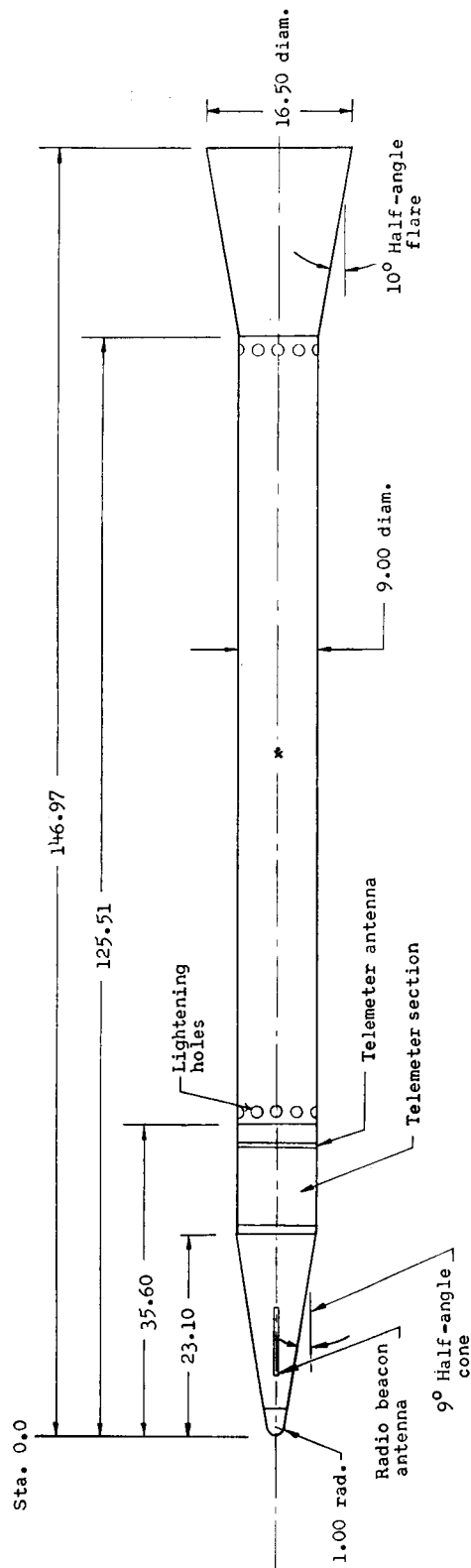
(a) General configuration. All dimensions are in inches.

Figure 7.- Payload stage.

25
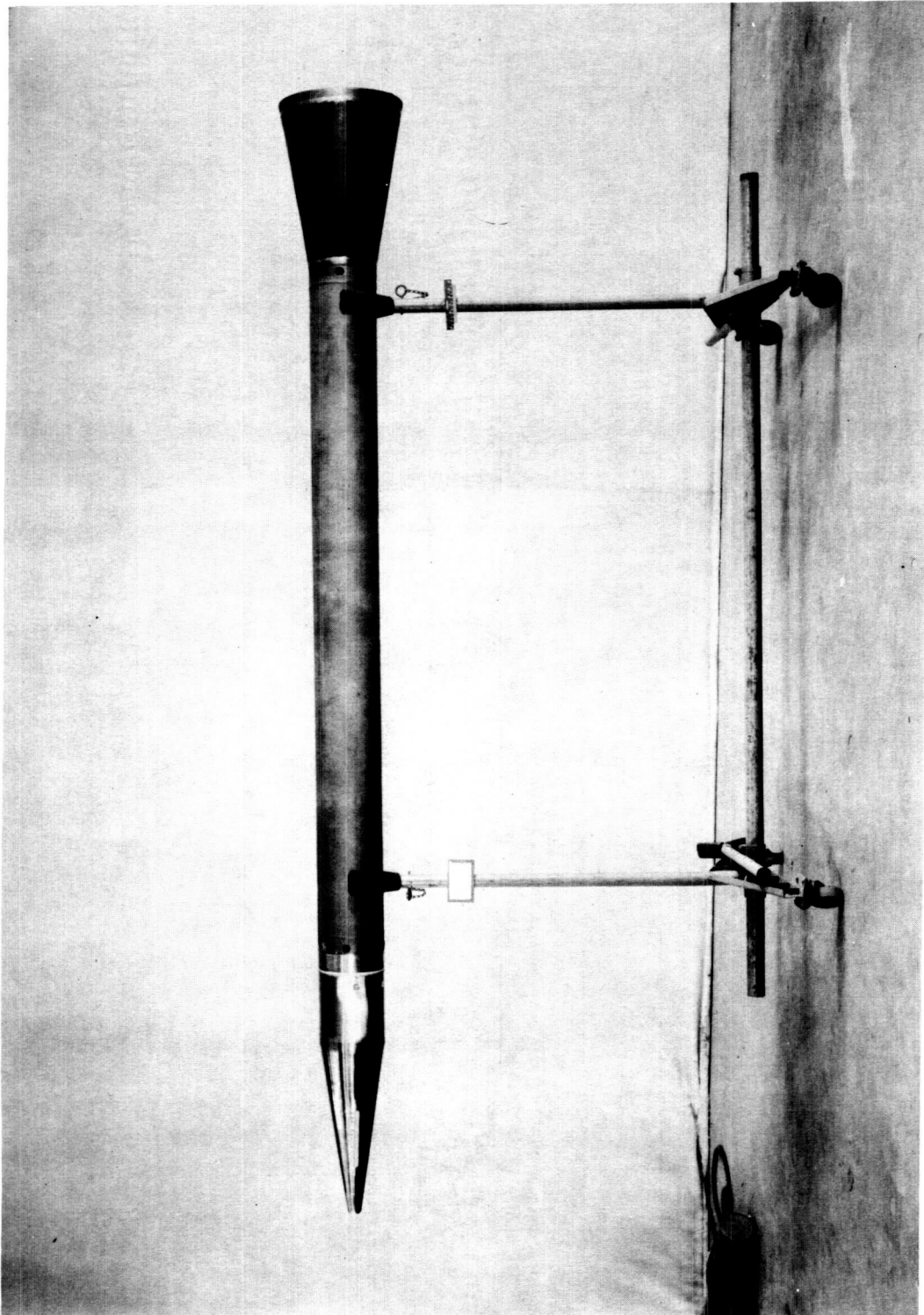
(b) Photograph of payload stage.   L-61-5792.1

Figure 7.- Concluded.
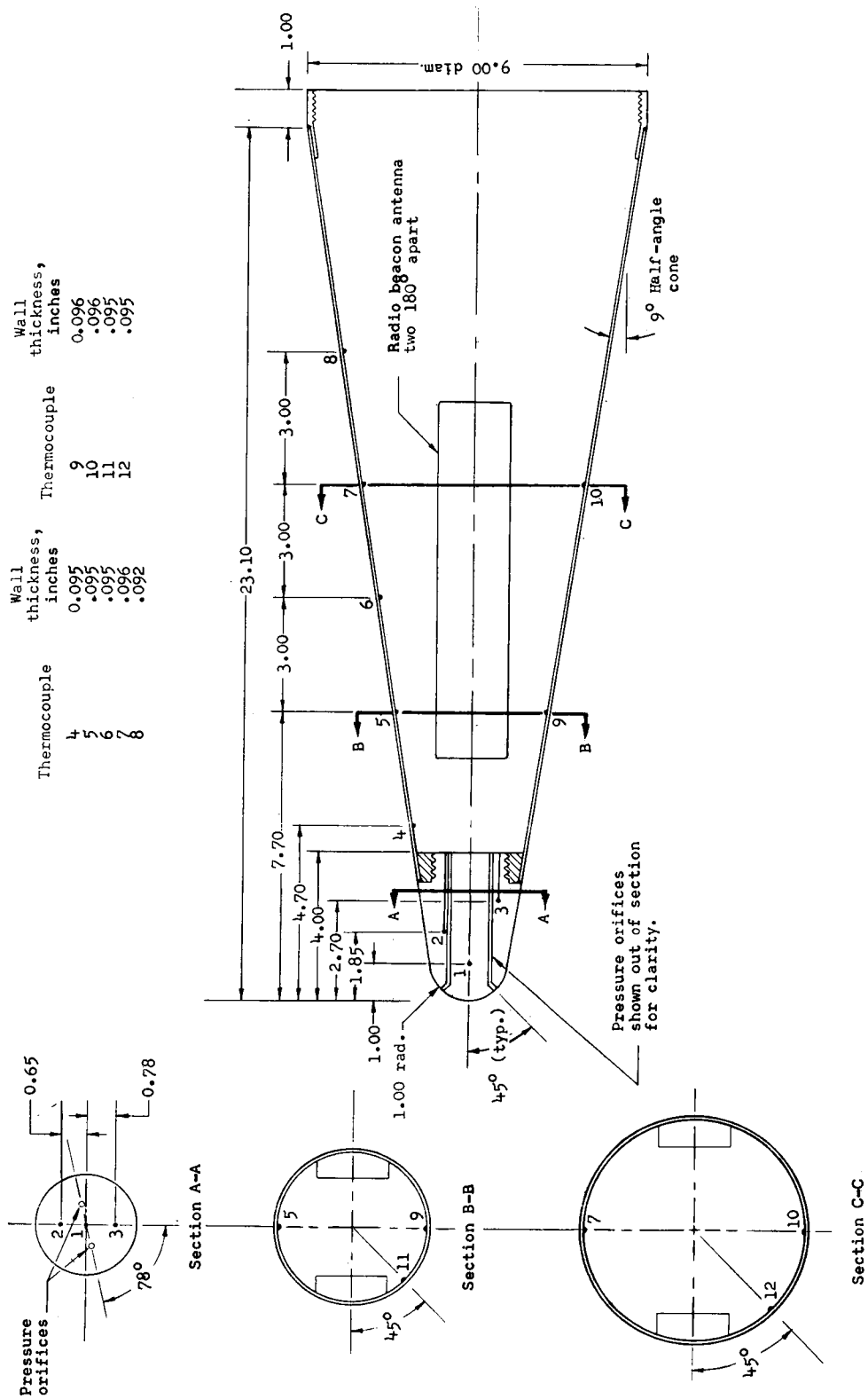
(a) Nose detail. All dimensions are in inches.

Figure 8.- Test nose.
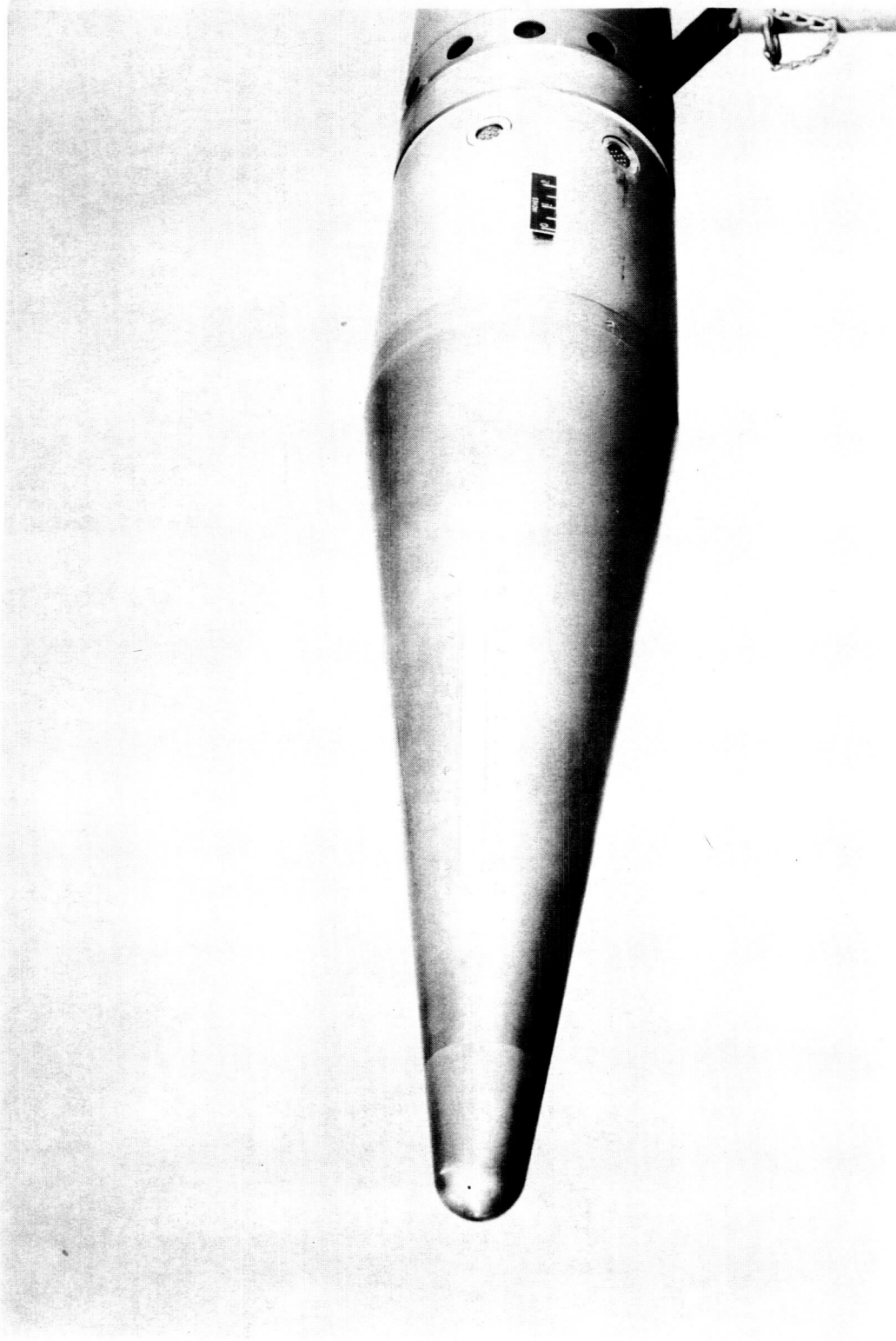
(b) Photograph of test nose.   L-61-5789

Figure 8.- Concluded.
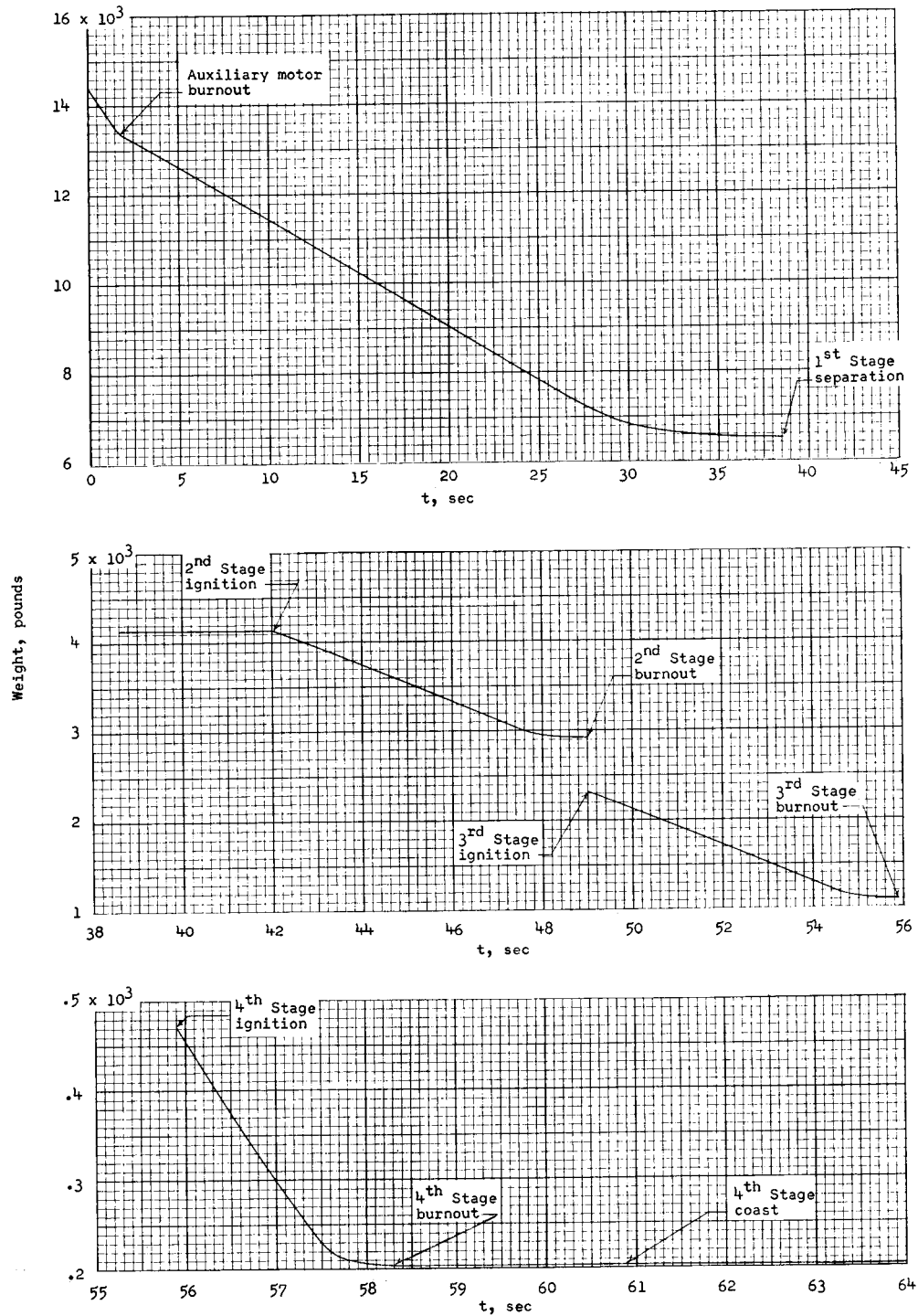
(a) Variation of weight with time.

Figure 9.- General properties of four-stage vehicle system.
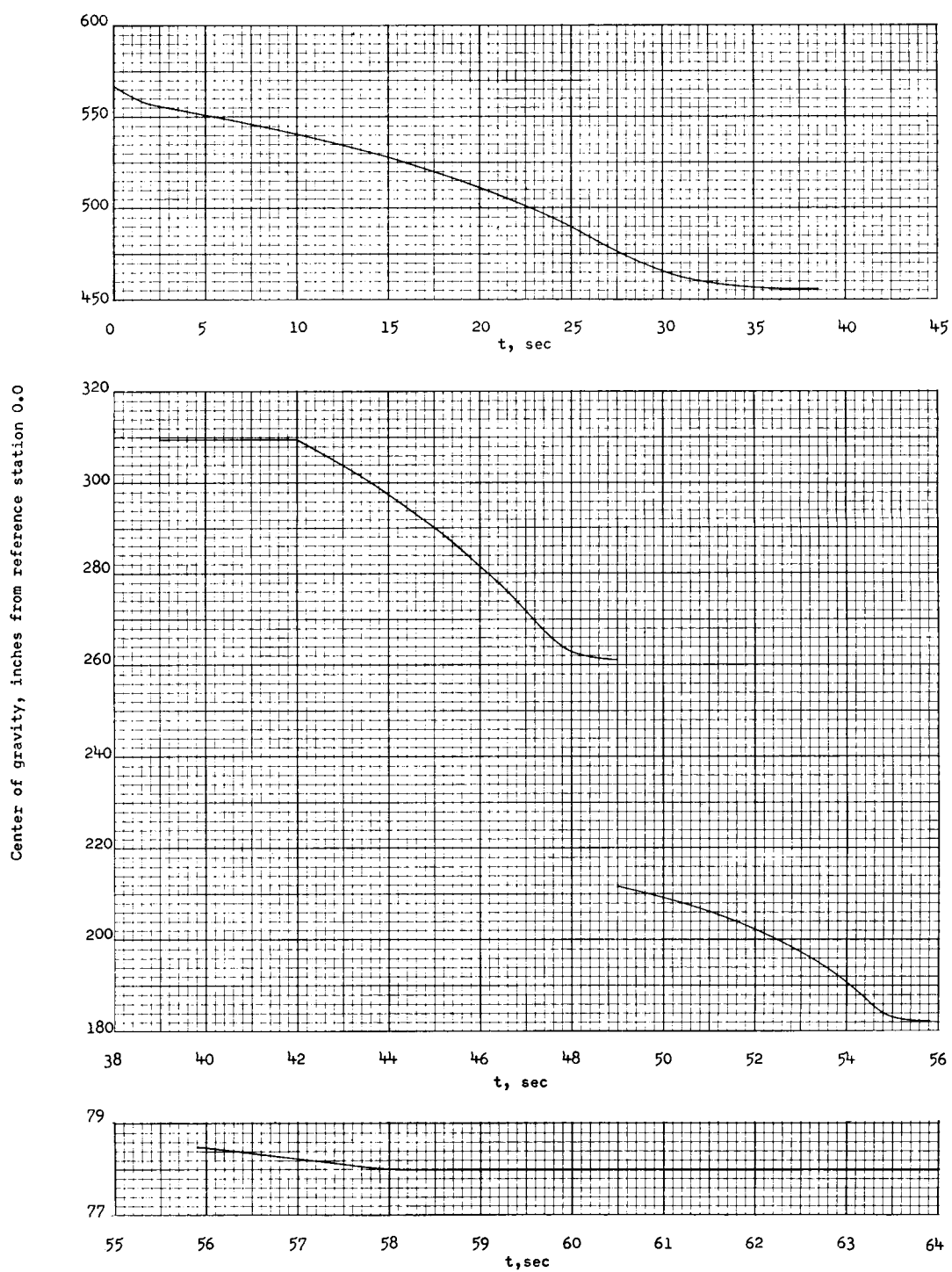
(b) Variation of center of gravity with time.

Figure 9.- Continued.
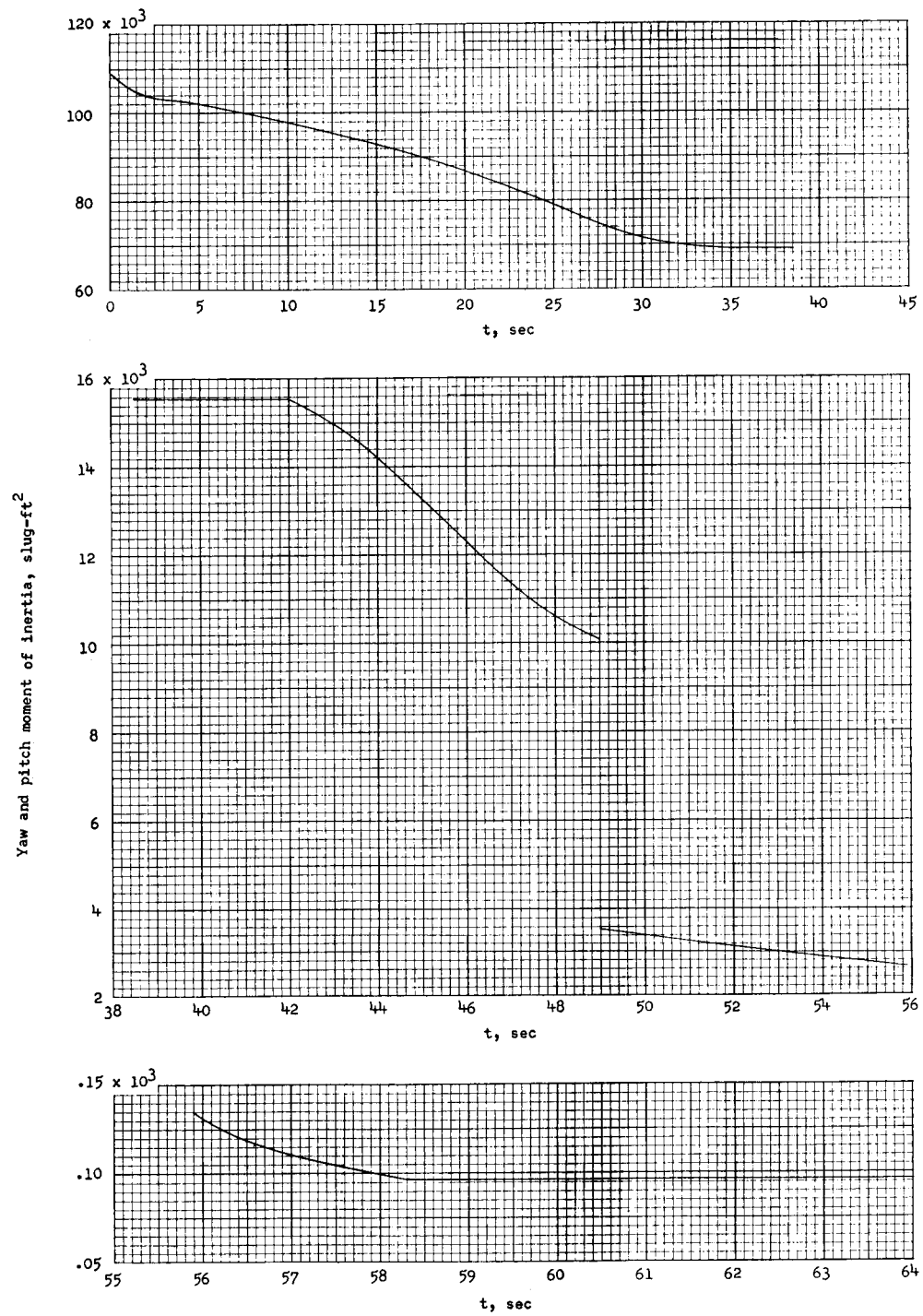
(c) Variation of moment of inertia in yaw and pitch with time.

Figure 9.- Continued.
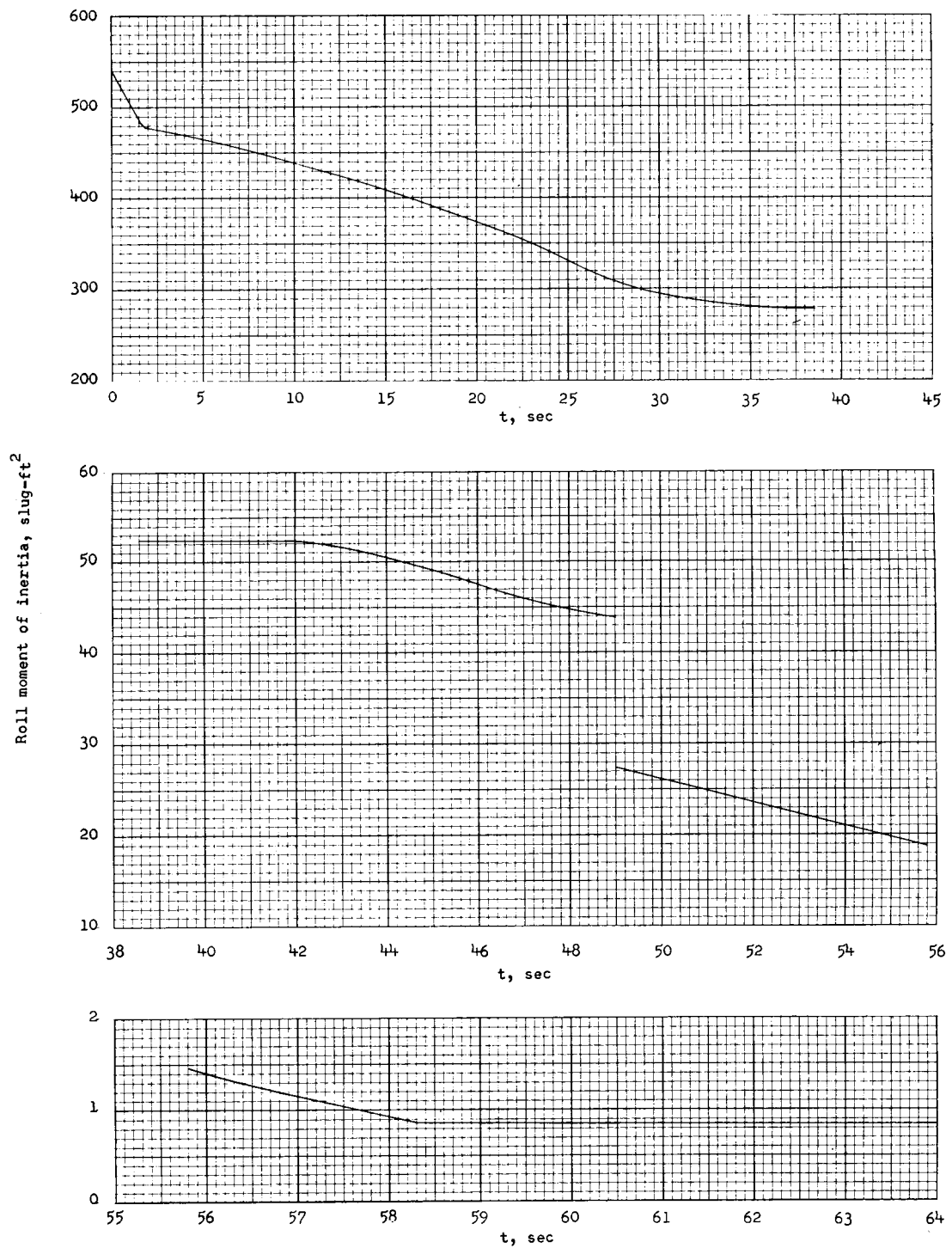
(d) Variation of roll moment of inertia with time.

Figure 9.- Concluded.
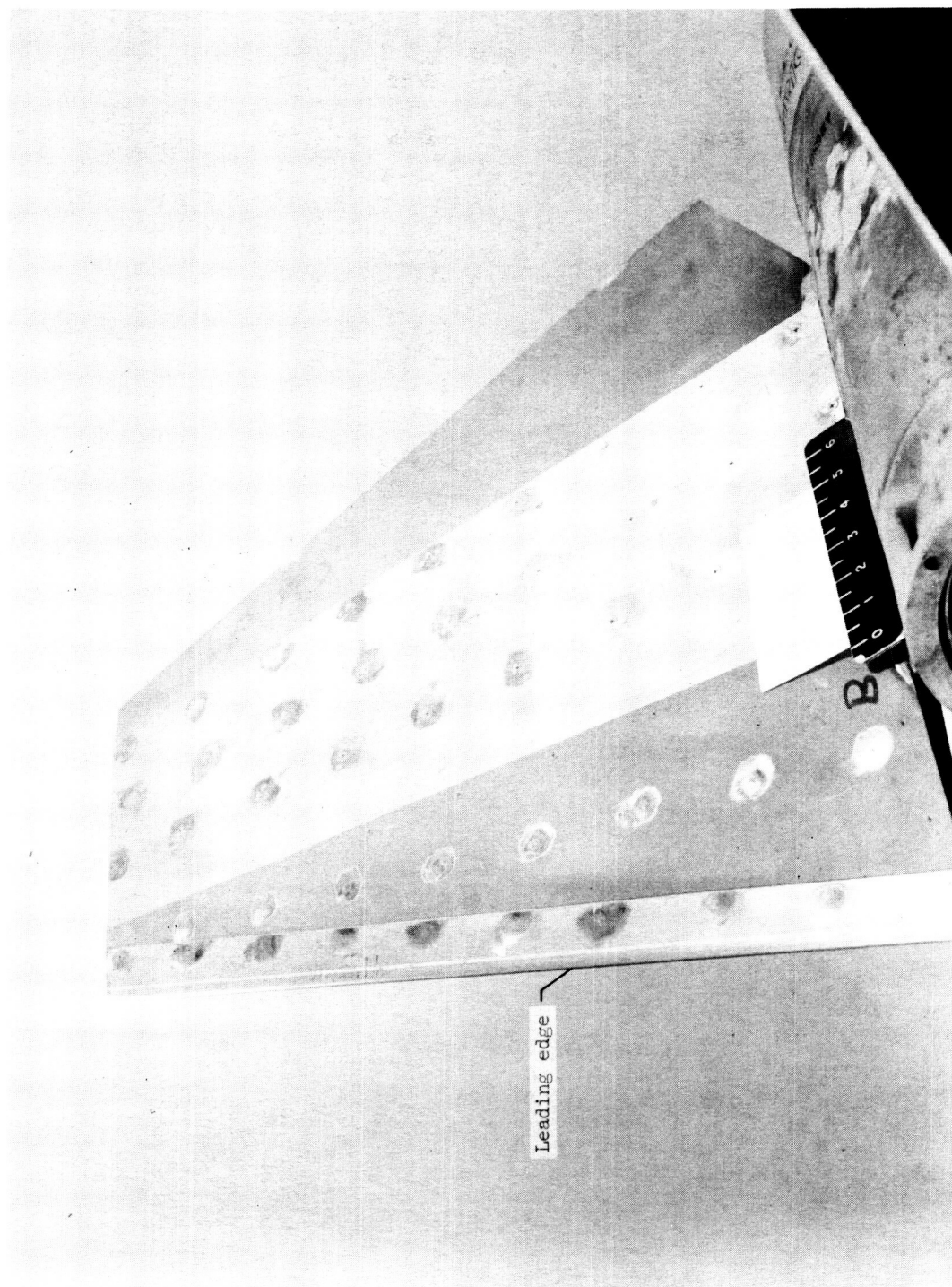
Leading edge

(a) Side view of second-stage fins.   L-61-3154.1

Figure 10.- Photographs of heat protection material on leading edges, leading-edge wedges, and flat sections of second- and third-stage fins.

Magnesium fin

Fiber-glass insulation

Inconel heat shield

Inconel wrap
leading edge
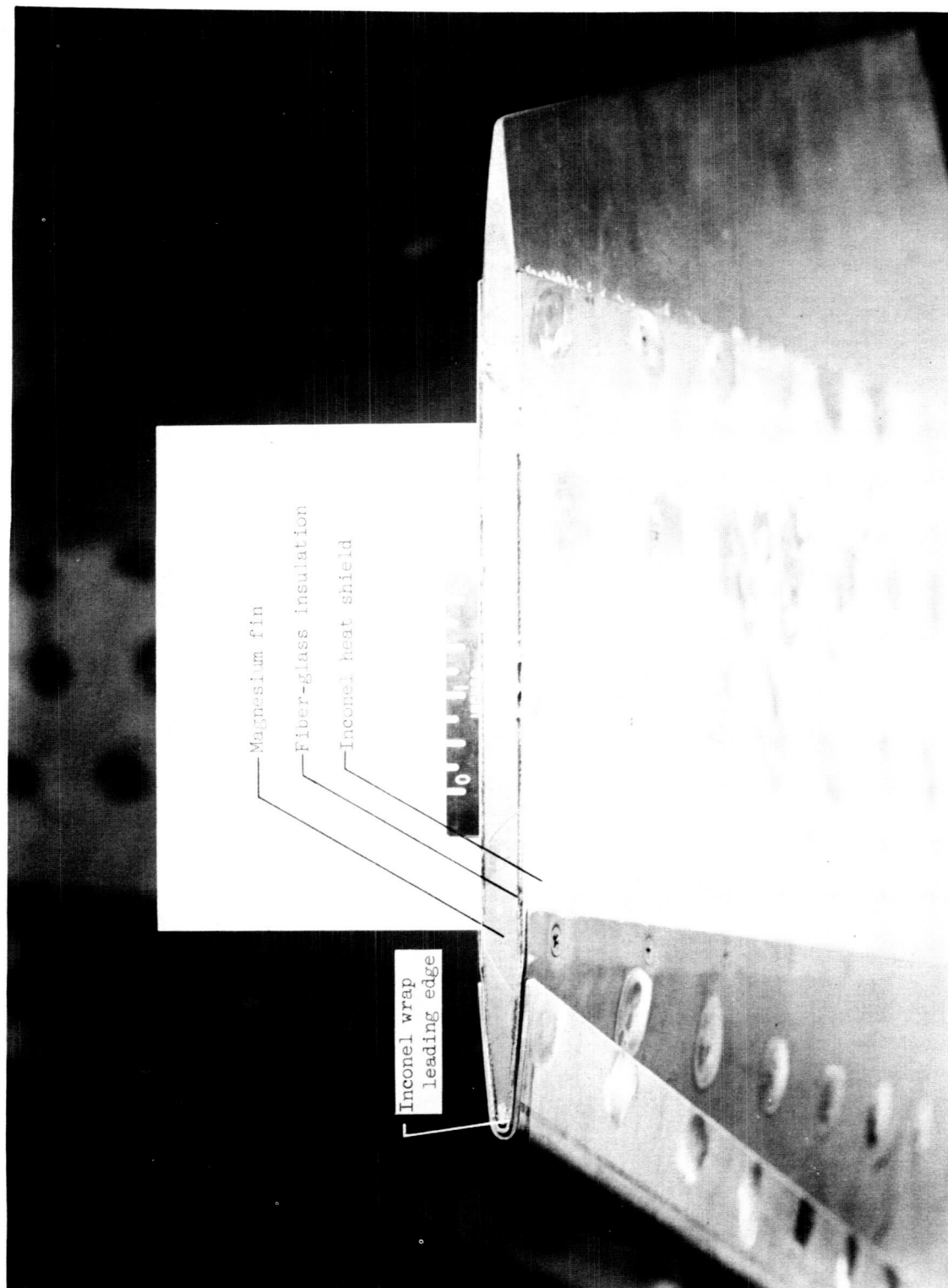
(b) Tip view of second-stage fins. L-61-3156.1

Figure 10.- Continued.

Leading edge
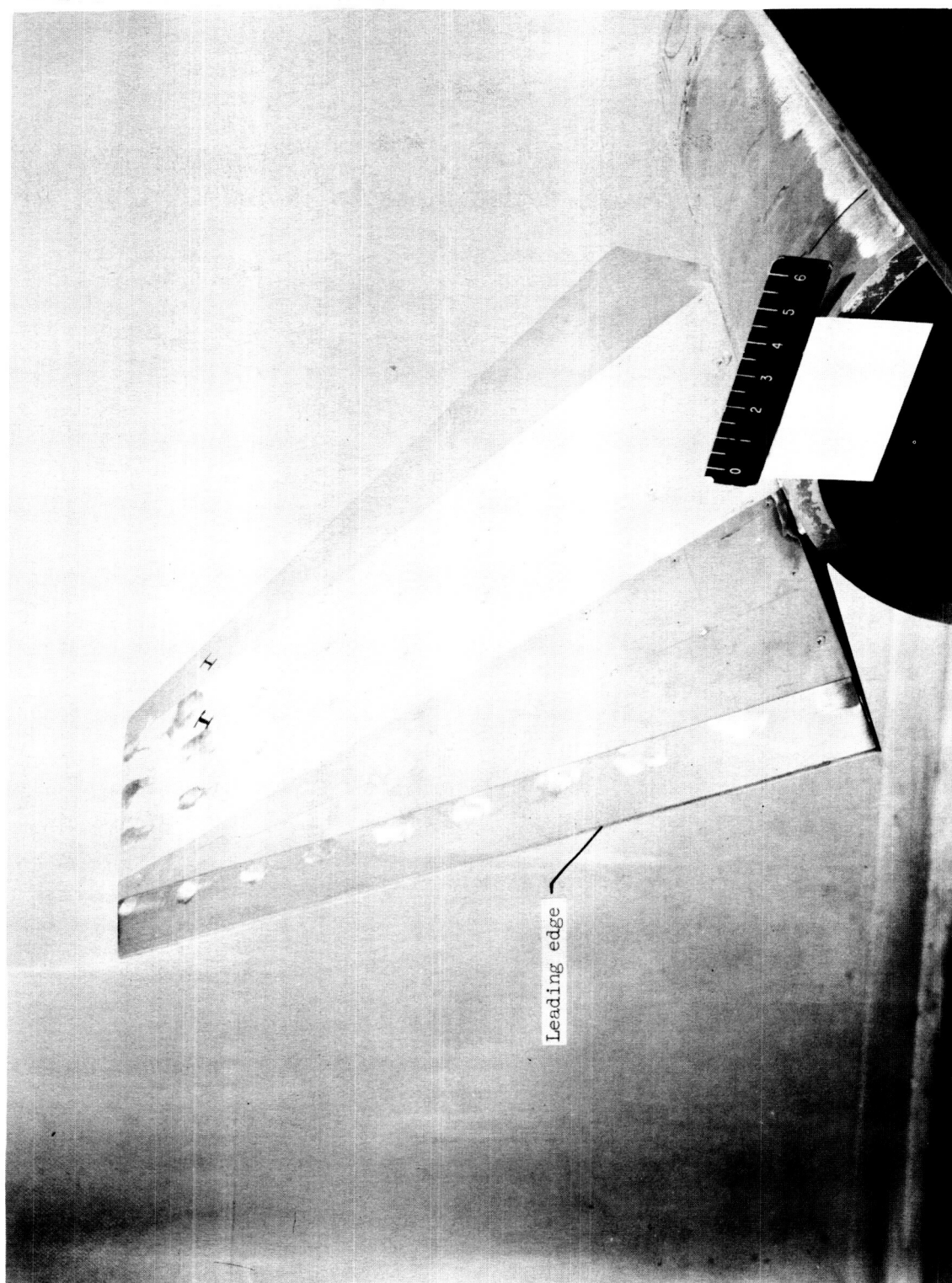
(c) Side view of third-stage fins. L-61-3152.1

Figure 10.- Continued.

Stainless-steel
leading edge

Air gap
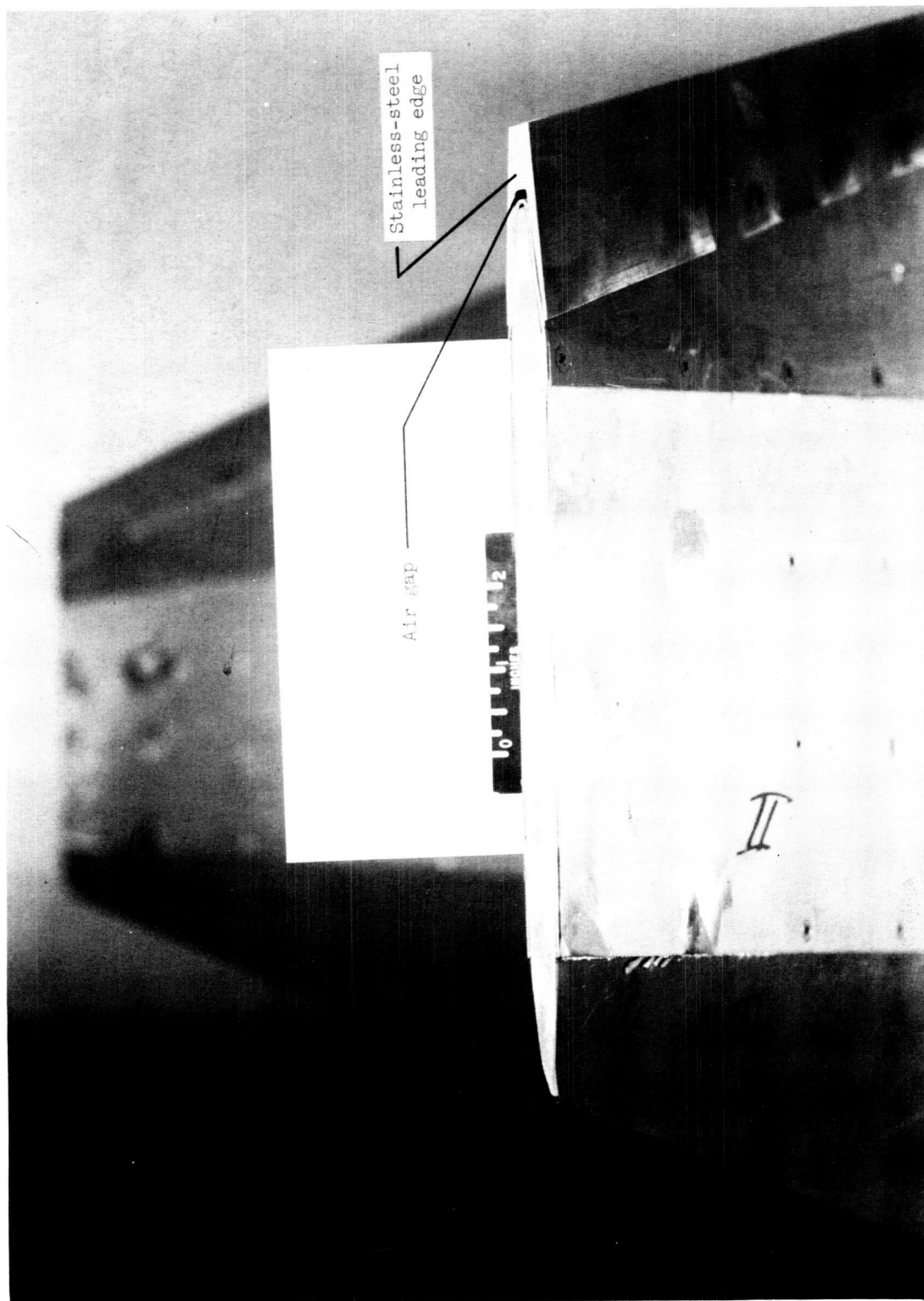
(d) Tip view of third-stage fins.   L-61-3157.1

Figure 10.- Concluded.

36
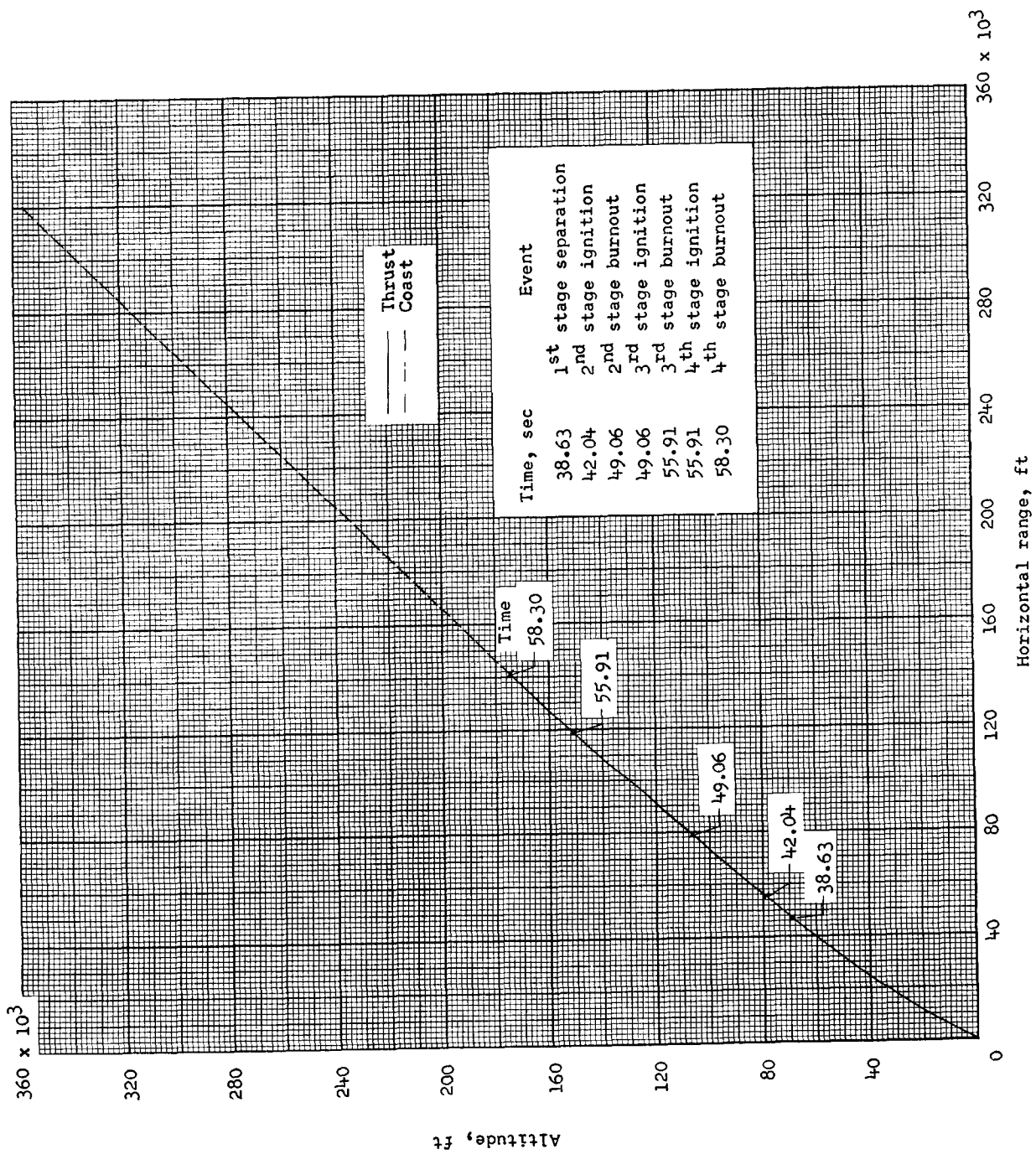
Figure 11.- Portion of flight trajectory.
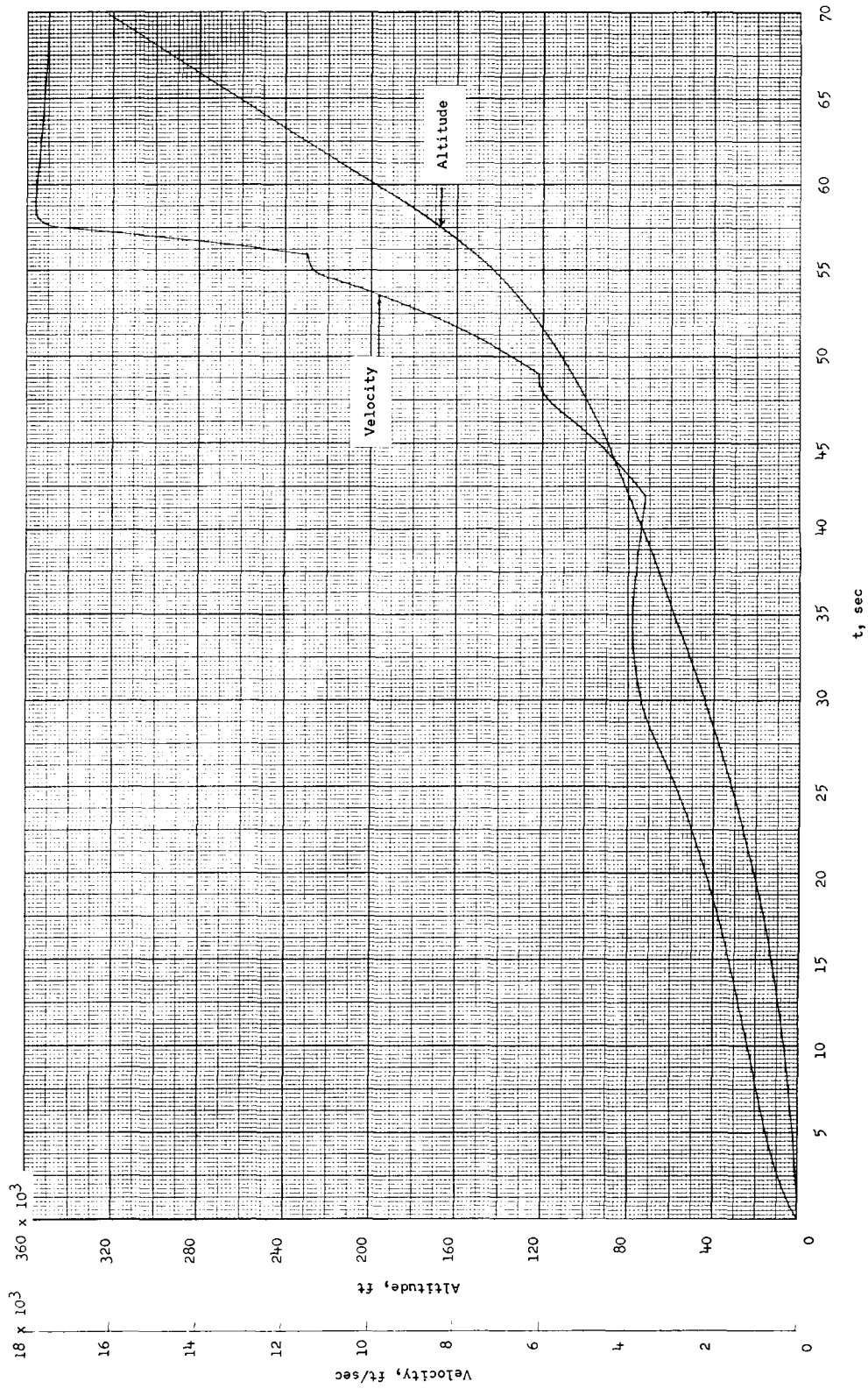
Figure 12.- Time histories of free-stream flight-test conditions of velocity and altitude.
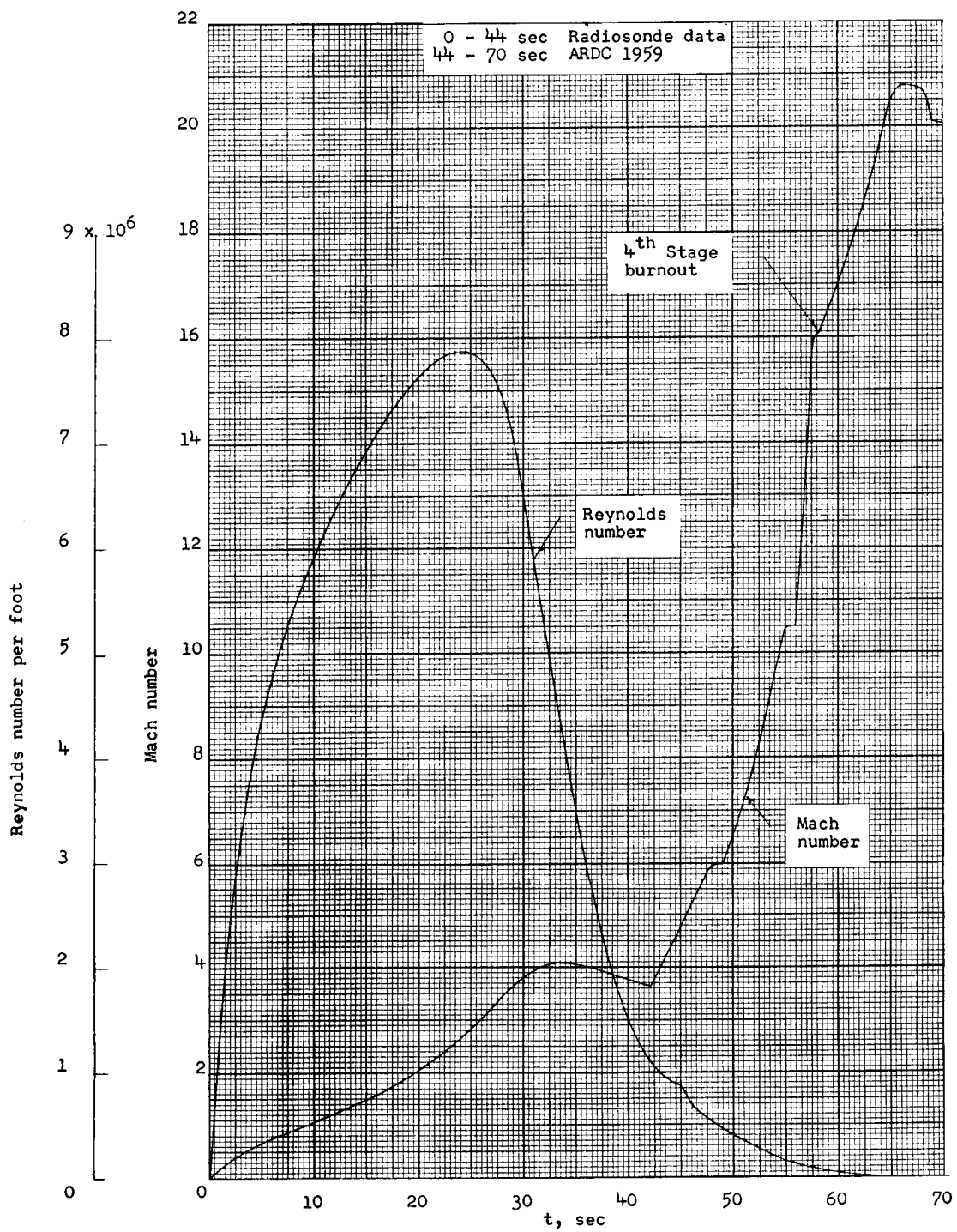
(a) Mach number and Reynolds number per foot.

Figure 13.- Time histories of flight-test environmental conditions.
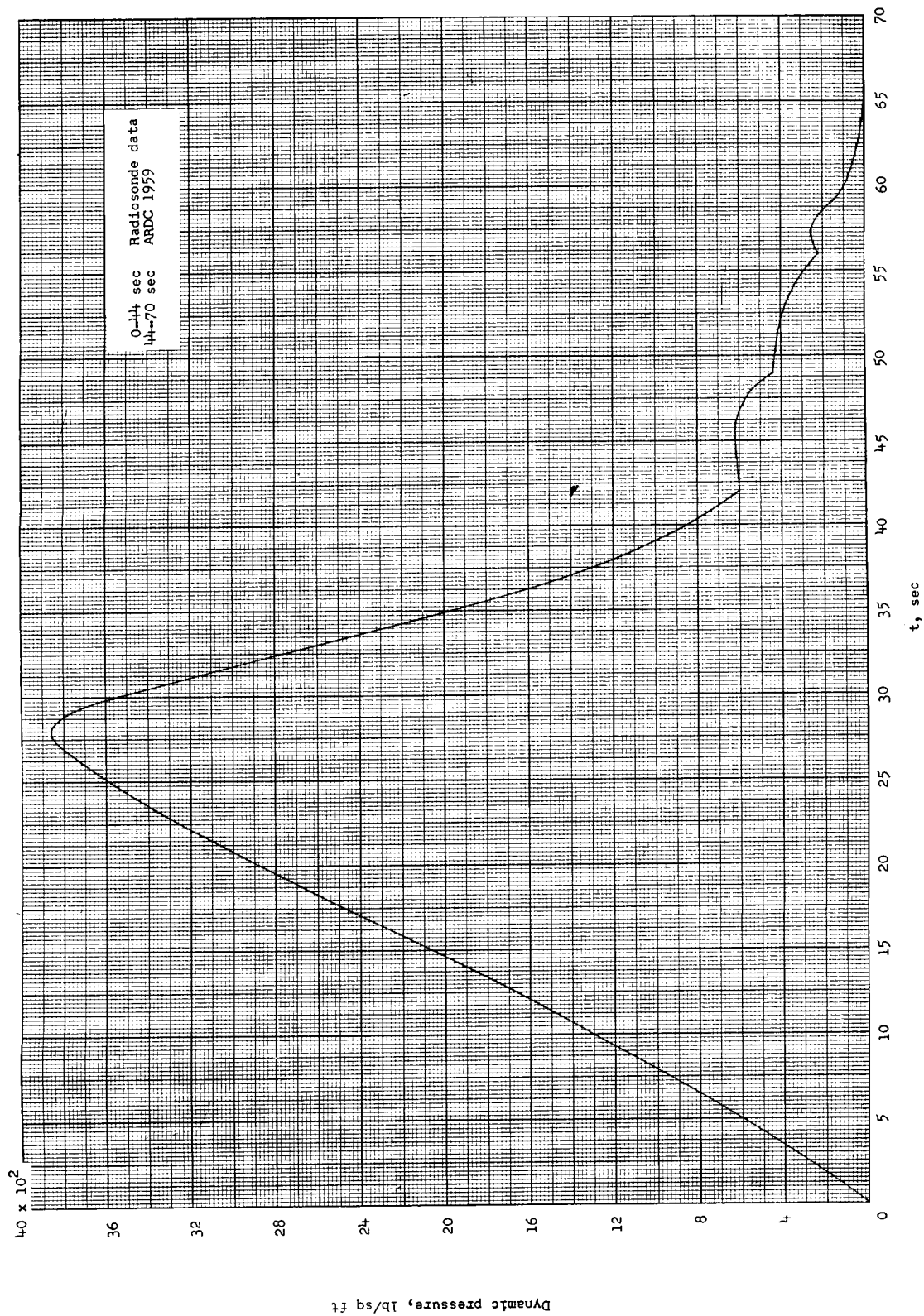
(b) Dynamic pressure.

Figure 13.- Concluded.
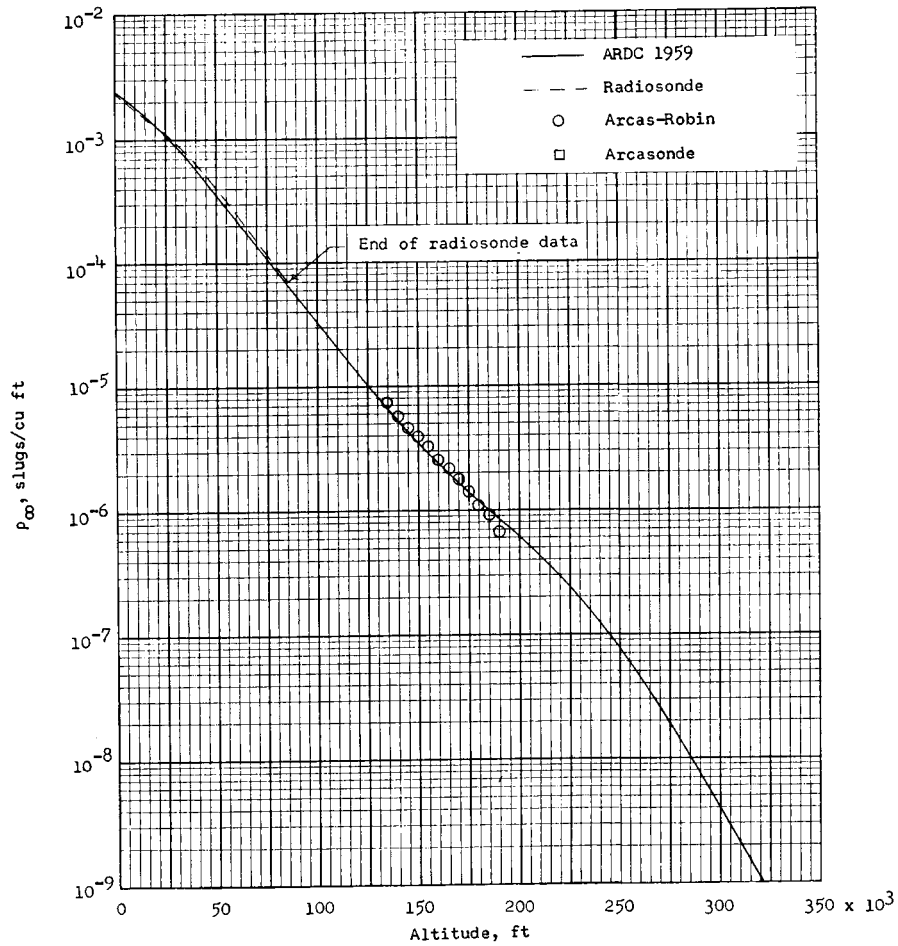
(a) Density variation with altitude.
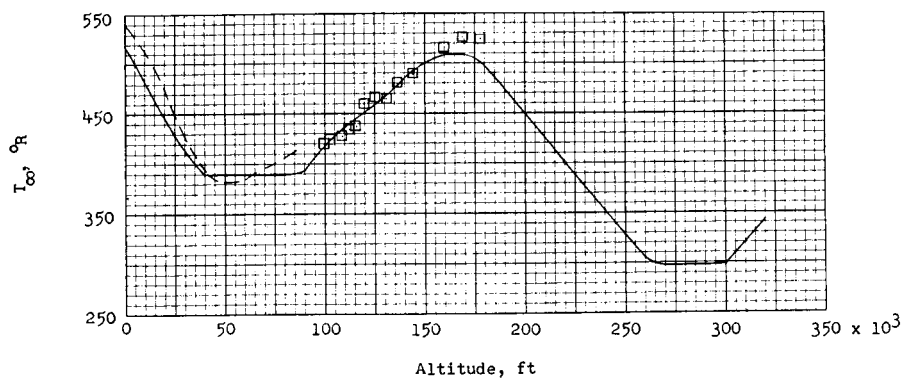
(b) Temperature variation with altitude.

Figure 14.- Comparison of density and temperature measurements with ARDC 1959 model atmosphere.

	Event		Time, sec	Event
Time, sec			49.06	3rd Stage ignition
38.63	1st Stage separation		55.91	3rd Stage burnout
42.04	2nd Stage ignition		55.91	4th Stage ignition
49.06	2nd Stage burnout		58.30	4th Stage burnout
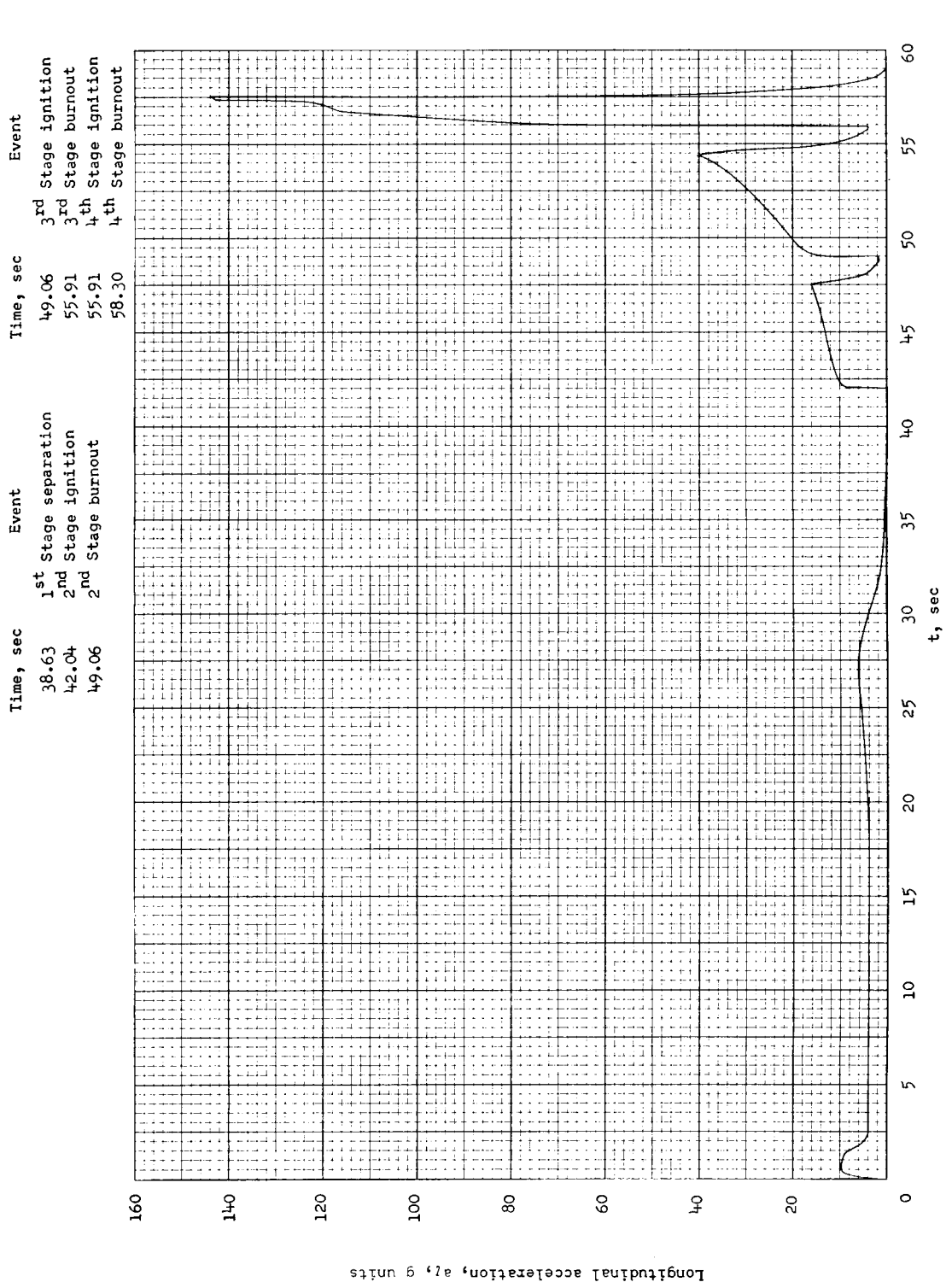
(a) Longitudinal acceleration.

Figure 15.- Time history of measured accelerations of four-stage vehicle system. (Accelerations not corrected for off-the-center-of-gravity locations.)

(b) Transverse and normal accelerations.

Figure 15.- Concluded.
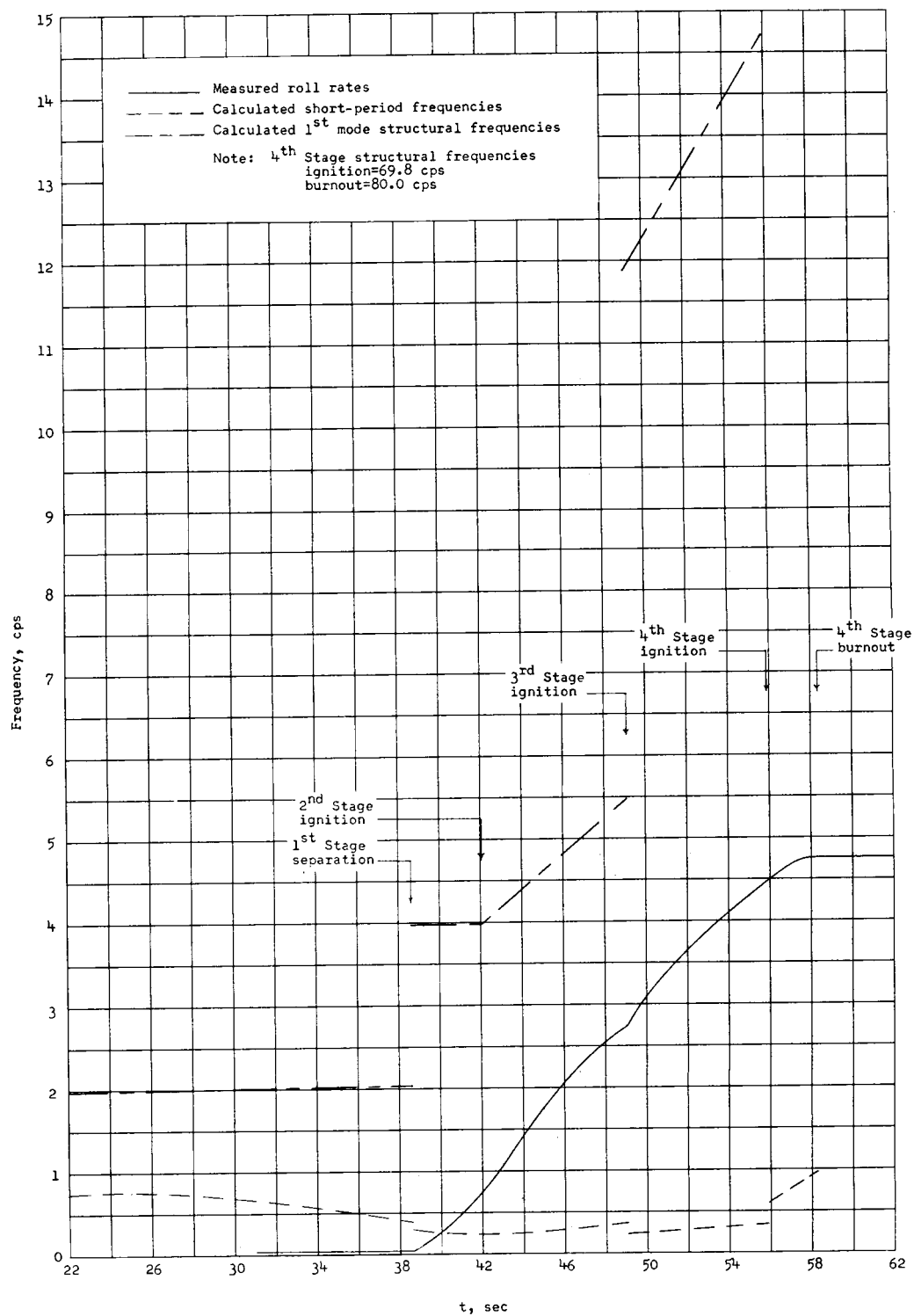
Figure 16.- Time histories of measured roll rates, calculated short-period pitch and yaw frequencies, and vehicle structural frequencies.

Time, sec	Event	Time, sec	Event
38.63	1st Stage separation	49.06	3rd Stage ignition
42.04	2nd Stage ignition	55.91	3rd Stage burnout
49.06	2nd Stage burnout	55.91	4th Stage ignition
		58.30	4th Stage burnout
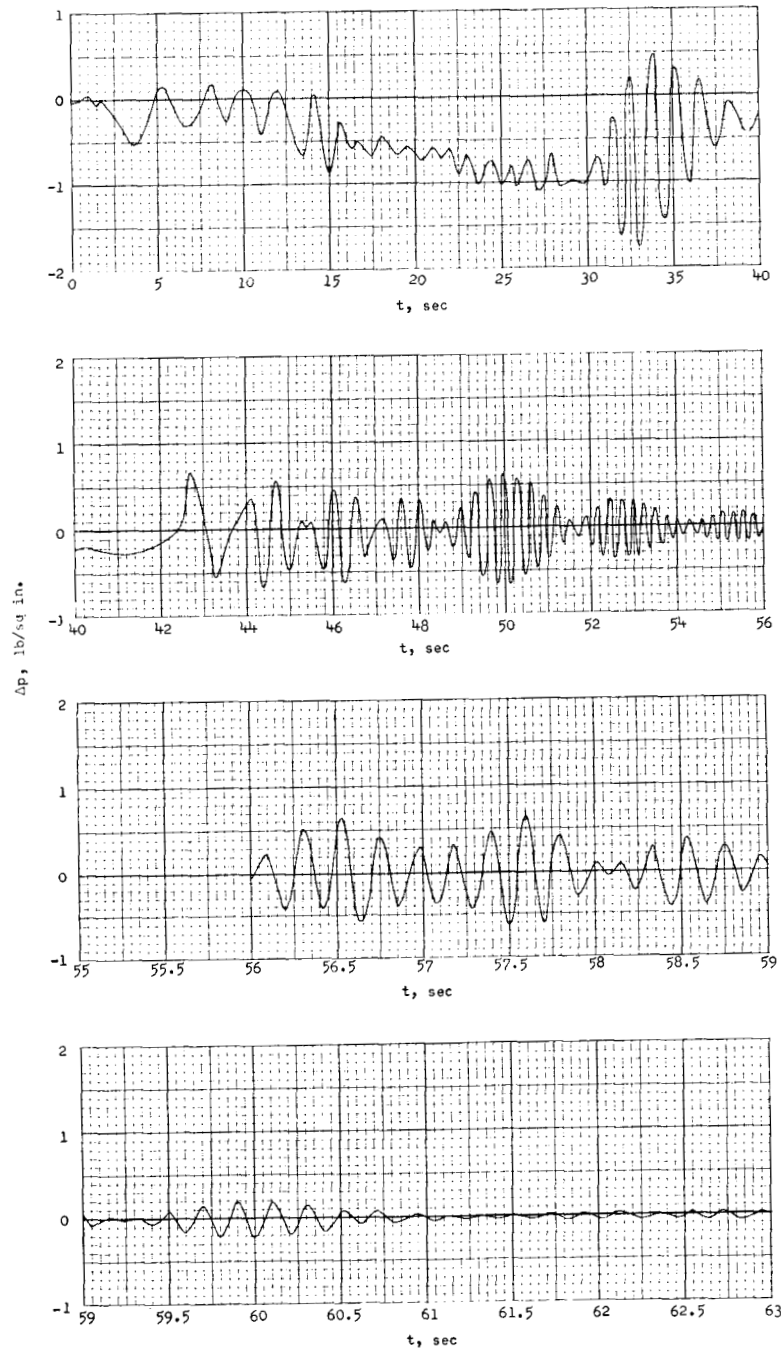
Figure 17.- Time variation of measured differential pressure.
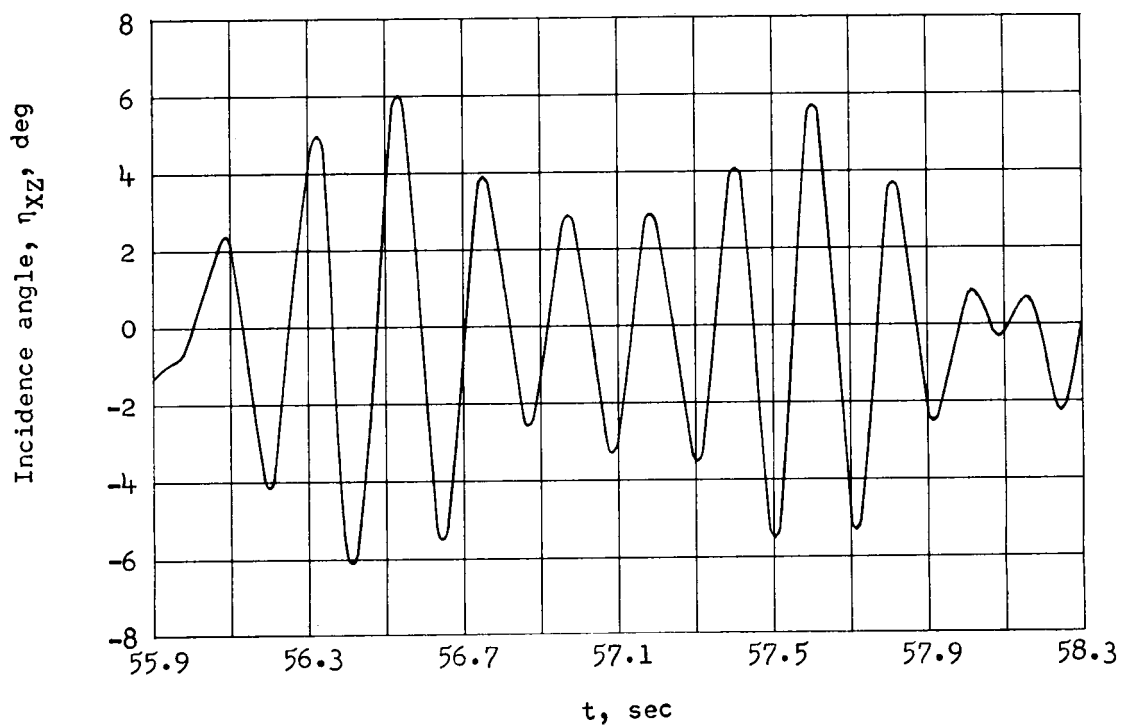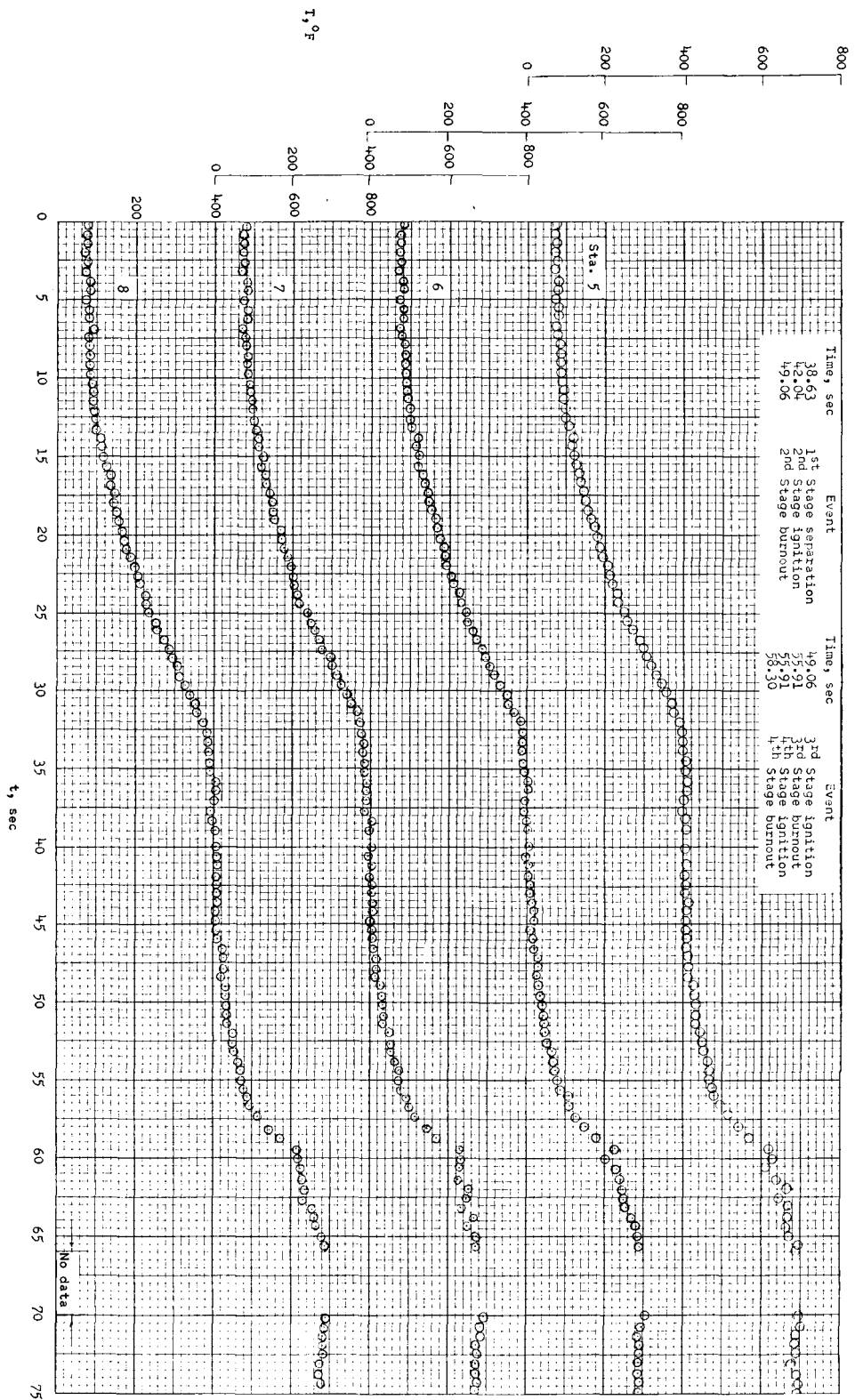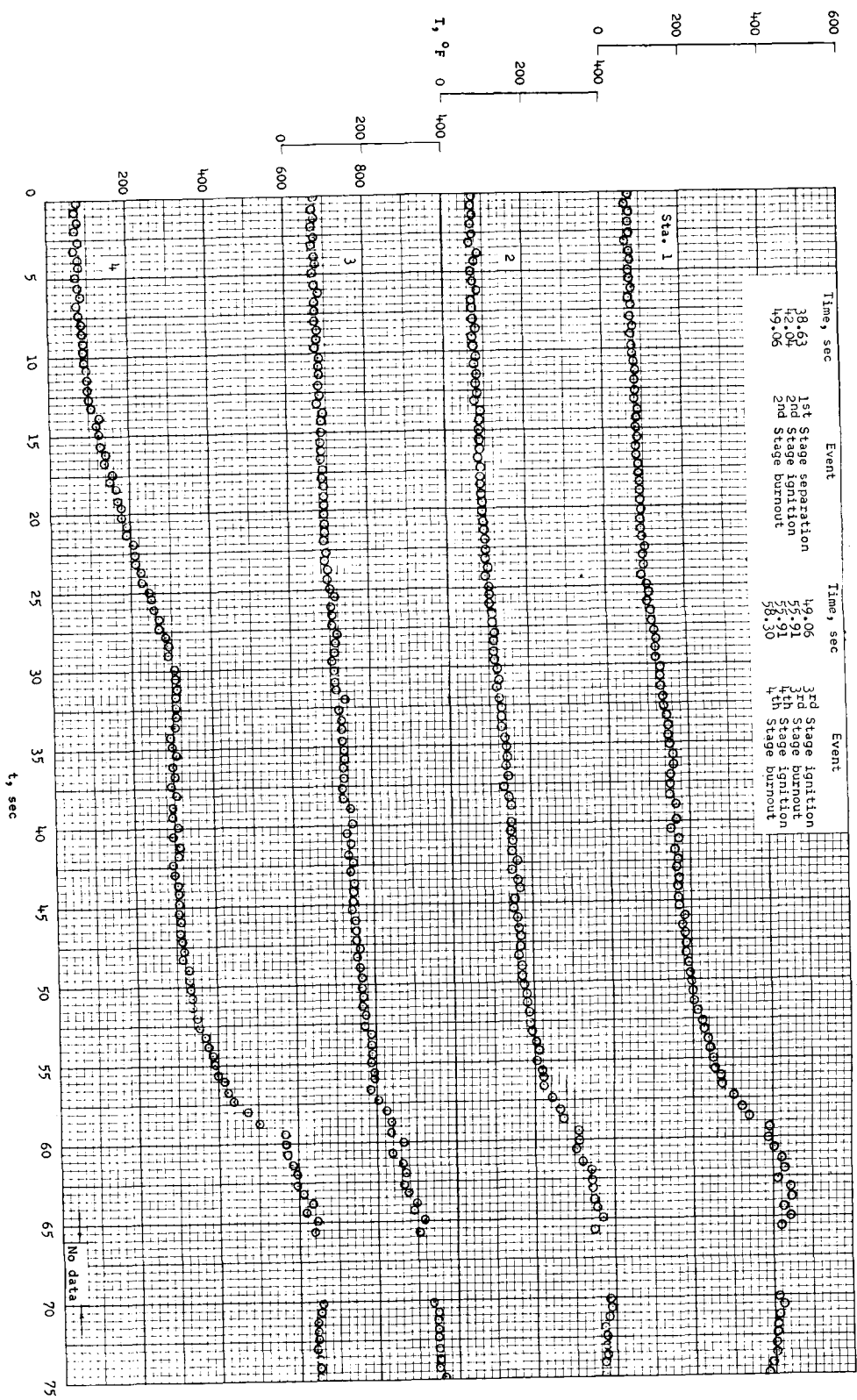
(a) Thrust period.
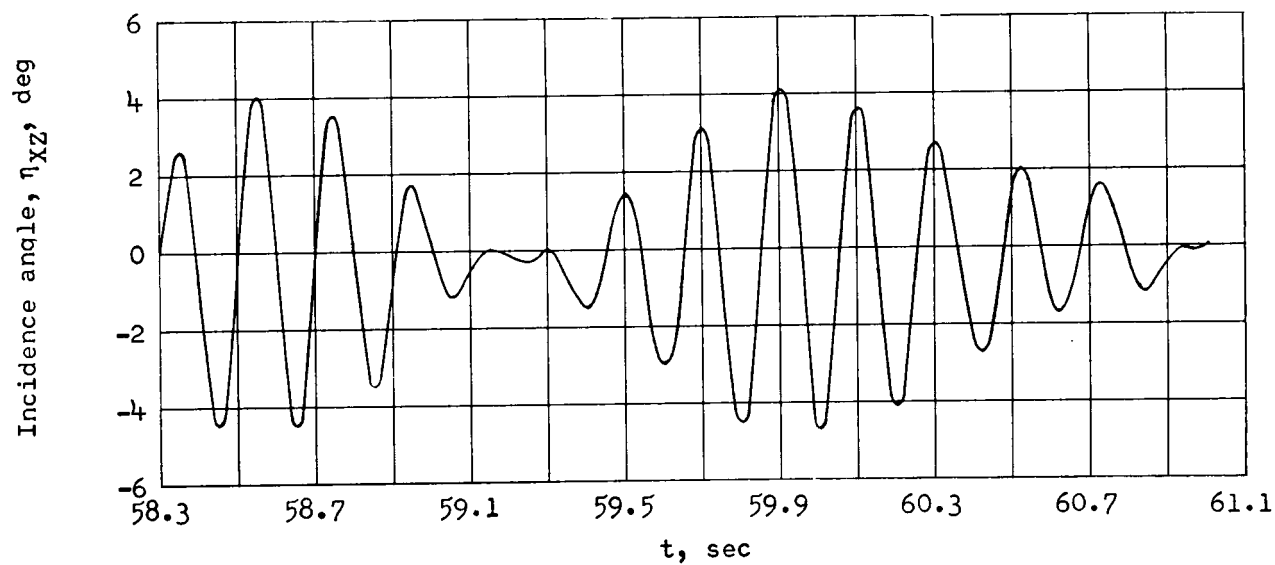
(b) Coast period.

Figure 18.- Time variation of angle of incidence in plane of pressure orifices of payload stage.
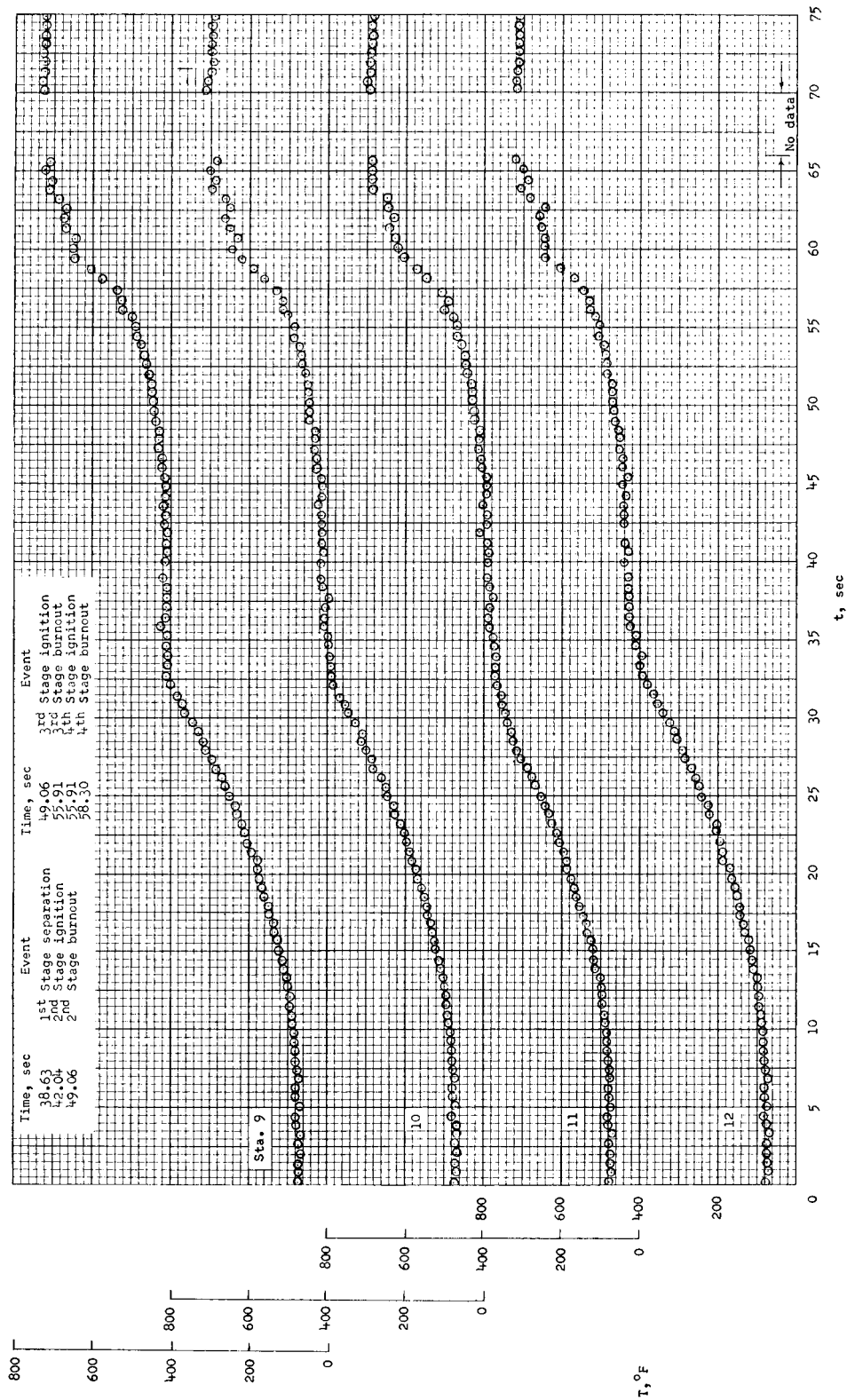
(b) Stations 5, 6, 7, and 8.

Figure 19.- Continued.

(a) Stations 1, 2, 3, and 4.

Figure 19.- Time histories of measured skin temperatures.

(c) Stations 9, 10, 11, and 12.

Figure 19.- Concluded.